Ocean Applications

6

M. Migliaccio, F. Nunziata, A. Marino, C. Brekke, and S. Skrunes

Abstract

In this chapter, the most promising techniques to observe oil slicks and to detect metallic targets at sea using polarimetric synthetic aperture radar (SAR) data are reviewed and critically analysed. The detection of oil slicks in SAR data is made difficult not only by the presence of speckle but also by the presence of, e.g. biogenic films, low-wind areas, rain cells, currents, etc., which increase the false alarm probability. The use of polarimetric features has been shown to both observe oil slicks and distinguish them from weak-damping look-alikes but also to extract some of their properties. Similarly to oil slicks, the same factors can hamper the detection of metallic targets at sea. The radiometric information provided by traditional single-channel SAR is not generally sufficient to unambiguously detect man-made metallic targets over the sea surface. This shortcoming is overcome by employing polarimetry, which allows to fully characterize the scattering mechanism of such targets.

6.1 Introduction

The two main ocean applications analysed are related to oil slicks and metallic target detection.

SAR oil slick observation is physically possible under low-to-moderate wind conditions (~3–12 m/s), because an oil slick damps the short gravity and capillary waves and reduces the friction velocity generating a region of low backscatter area in the SAR image. However, SAR oil slick detection is not an easy task, since SAR images are affected by multiplicative noise, known as speckle, which hampers interpretability of such images. Furthermore, there are other physical phenomena, known as look-alikes, which can generate dark areas in SAR images not related to oil slicks, such as biogenic films (e.g. slicks produced by animals and plankton), low-wind areas, areas of wind-shadow near coasts, rain cells, currents, zones of upwelling, internal waves and oceanic or atmospheric fronts. Tailored filtering techniques must be developed in order to minimize the number of false alarms. Within such a context, single-polarization SAR oil slick detection procedures can be generally divided into three phases: dark area detection, feature extraction and oil slick/look-alike classification. On the basis of the estimated features and some a priori knowledge, it is possible to assign a probability that a dark area is an oil slick. Furthermore, the usefulness of additional external data is recognized to enhance the ability to distinguish between oil slicks and look-alikes, such as local wind field information (to sort out low-wind areas) and optical data to identify biogenic films. Recently, the superiority of polarimetric SAR measurements for sea oil slick observation purposes has been demonstrated. New quad- and dual-polarimetric approaches have been recently developed for sea oil slick observation, under low-to-moderate wind conditions, and are here considered.

Polarimetric models and analysis tools have been developed to observe sea oil slicks and have shown that some polarimetric features, namely, HH-VV correlation, unpolarized backscattered energy and scene depolarization capabilities, can be successfully used to both observe oil slicks and distinguish them from weak-damping look-alikes (Nunziata et al. 2012a; Solberg 2012).

With respect to the state of the art related to SAR observation of man-made metallic targets at sea, both image- and physically based approaches have been developed. The electromagnetic wave scattered off man-made metallic targets at sea is physically determined by several scattering

M. Migliaccio (✉) · F. Nunziata
Dipartimento di Ingegneria, University of Naples "Parthenope", Naples, Italy
e-mail: m.m@uniparthenope.it

A. Marino
Biological and Environmental Sciences, University of Stirling, Stirling, UK

C. Brekke · S. Skrunes
UiT the Arctic University of Norway, Tromsø, Norway

I. Hajnsek, Y.-L. Desnos (eds.), *Polarimetric Synthetic Aperture Radar*, Remote Sensing and Digital Image Processing 25,
https://doi.org/10.1007/978-3-030-56504-6_6

mechanisms that cause a high coherent microwave response depending on the construction material and the characteristics of the radar instrument, such as incidence angle, frequency, polarization, resolution and speckle. Accordingly, ships and oil rigs, hereinafter man-made metallic targets, appear in SAR images as bright spots over a dark marine background. Following this rationale, many image-based techniques have been developed which seek for anomalies in SAR images. However, SAR observation of man-made metallic targets at sea is a nontrivial task due to speckle and natural physical processes, e.g. atmospheric fronts, internal waves, current boundaries, breaking waves, outlying rocks, shoals, sea currents, coastal effects, etc., which may generate false alarms. Accordingly, man-made metallic targets detection is a complex topic that can hardly be optimized with conventional single-polarization SARs. Radiometric information provided by traditional single-channel SAR is not generally sufficient to unambiguously detect man-made metallic targets over the sea surface, since it does not fully characterize the scattering mechanism of such targets. Hence, new polarimetric approaches have been developed for man-made metallic targets observation at sea that perform better than the single-polarization ones.

In this chapter the most promising polarimetric techniques to observe oil slicks and to detect metallic targets at sea are reviewed and critically analysed.

6.2 Oil at Sea Observation

6.2.1 Introduction, Motivation and Literature Review

Oil at sea observation has received considerable attention in recent literature due to its impact on marine ecosystems, fisheries, wildlife, etc. SAR has proven to be a fundamental remote sensing tool for oil slick mapping, under low-to-moderate wind conditions (3–15 m/s), due to its almost all-weather and its all-day imaging capabilities. In very simple terms, the physical rationale underpinning SAR oil slick observation resides on its viscoelastic properties that damp the short Bragg resonant waves resulting in a low backscatter area, i.e. a dark patch in the SAR image plane.

Marine slicks are composed of two major types of hydrocarbons, mineral oils including petroleum-based material and films from biological processes. Mineral oils are typically due to spills from ships and offshore drilling platforms and pipelines, natural hydrocarbon seeps and discharge from storm-water urban run-off. Mineral oils spread into thin layers through gravity and surface tension and evaporate through weather over time. Biogenic films, also called surfactants (surface-active agents) or natural films, are a viscous by-product of ocean plant and animal growth and decay.

Traditionally, SAR oil slick observation is based on single-polarization VV or HH intensity images, and manual inspection is very often still needed (Solberg 2012).

With polarimetric SAR sensor capabilities now operationally available, several polarimetric techniques have been proposed for oil slick monitoring showing superiority with respect to single-polarization SAR cases (Nunziata et al. 2012a; Solberg 2012). Here, a brief review of the most up-to-date polarimetric techniques to observe oil at sea is provided. Then, some of the most promising polarimetric techniques are applied to selected test cases in order to clearly show the benefit of polarimetric SAR data for oil at sea observation.

Polarimetric models and analysis tools have been developed to observe sea oil slicks and have shown that some polarimetric features, namely, the correlation between the co-polarized (HH and VV) channels, unpolarized backscattered energy and scene depolarization capabilities, can be successfully used to both observe oil slicks and distinguish them from weak-damping look-alikes (Nunziata et al. 2012a). All these approaches share a common physical rationale that relies on the fact that, under low-to-moderate wind conditions (3–12 m/s) and at intermediate incidence angles, both slick-free and weak-damping slick-covered sea surfaces call for Bragg scattering, whereas in the case of oil-covered sea surfaces, a completely different one, i.e. non-Bragg scattering mechanism, is in place. Following this rationale, these polarimetric features, which can be considered as measures of the departure from Bragg scattering, have been estimated by either the scattering **S**, the Kennaugh **K** or the coherency **T** matrices and have been successfully used to observe sea oil slicks in polarimetric SAR data (Nunziata et al. 2012a). A brief description of the state of the art related to polarimetric SAR data for oil at sea observation is provided as follows.

In Migliaccio et al. (2011a)), the benefits of polarimetric RADARSAT-2 SAR data to observe the Deepwater Horizon oil spill were shown using polarimetric features. In Minchew et al. (2012)) and Migliaccio and Nunziata (2014)), polarimetric features were extracted from L-band UAVSAR full-polarimetric SAR data to observe the oil slicks due to the Deepwater Horizon accident in Gulf of Mexico. It was shown that the dominant scattering mechanism, both over the slick-free and the slick-covered sea surface, is the tilted-Bragg scattering. In Jones et al. (2011)), polarimetric UAVSAR data collected over the polluted area of the Gulf of Mexico were exploited to observe oil-affected wetlands in Barataria Bay, Louisiana. In Nunziata et al. (2008)), a model to interpret the elements of the Mueller matrix in terms of sea surface scattering with and without oil slicks was developed. In Nunziata et al. (2011)), the co-polarized signature, i.e. the plot of the synthesized normalized radar cross section (NRCS) as a function of ellipticity and orientation angle, was exploited to observe oil at sea. The pedestal of the

signature is shown to be both able to observe oil at sea and distinguish them from weak-damping look-alikes. In Migliaccio et al. (2009a)), multi-polarization features were exploited to conceive a polarimetric processing chain to both observe oil slicks and distinguish them from weak-damping look-alikes. In Zhang et al. (2011)), full-polarimetric SAR data were used to observe oil seeps in the Gulf of Mexico. In Migliaccio et al. (2009b) and Velotto et al. (2011)), the standard deviation of the co-polarized phase difference (CPD) was shown to result in larger values over oil-covered areas and in very low values over both free sea surface and over biogenic slicks. In Migliaccio et al. (2011b)), the CPD approach was used together with a target detection approach, based on HH-HV SAR data, to conceive a processing chain able to observe both oil slicks and metallic targets at sea; i.e. oil field, in an unsupervised way.

6.2.2 Methodology

In this section the theoretical background behind the operational procedures is briefly described, starting from quad-polarimetric approaches and, then, moving to the dual-polarimetric one. To provide an effective physical description, the section presents a brief description of the polarimetric model that describes sea surface scattering with and without oil slicks, which is the backbone of the selected polarimetric approaches.

Under low-to-moderate wind conditions and at intermediate incidence angles, two reference scenarios must be distinguished: sea surface with and without oil slicks.

Slick-free sea surface scattering calls for Bragg or tilted-Bragg scattering. It is a single-reflection scattering mechanism that, being quasi-deterministic, is expected to be characterized by a low polarimetric entropy, a high correlation between like-polarized channels and a low unpolarized backscattered energy, as demonstrated in Nunziata et al. (2012a)). Similar polarimetric scattering features apply when dealing with weak-damping surfactants; e.g. biogenic slicks, some marine features, etc. In real cases, illegal oil discharges are typically heavy oils that do not belong to this class.

An oil-covered sea surface, due to the strong damping properties of oil slicks, dampens the short Bragg scattering waves generating a low backscatter area (i.e. a dark area in single-pol SAR images). From a polarimetric viewpoint, this means a large departure from the Bragg scattering mechanism (Nunziata et al. 2012a). In detail, a low correlation between like-polarized channels and a large unpolarized backscattered energy (which indicates that a high random scattering mechanism is in place) is expected, as demonstrated in Nunziata et al. (2012a)).

Following this rationale, polarimetric features, which can be considered as measures of the departure from Bragg scattering, have been successfully used to observe sea oil slicks in polarimetric SAR data. All the polarimetric features can be derived by the second-order products of the scattering matrix; i.e. either the coherency $\mathbf{T}$ or the covariance $\mathbf{C}$ matrix can be used. In this study the following polarimetric features are used: polarimetric entropy (H), modified anisotropy (A_{12}) (Wenguang et al. 2010), the mean scattering parameter $\overline{\alpha}$, normalized pedestal height (NP) (Nunziata et al. 2012a), conformity coefficient (Zhang et al. 2011) μ and standard deviation of the co-polarized phase difference (σ) (Migliaccio et al. 2009b). According to theoretical modelling, those polarimetric features are expected to follow the behaviour synthesized in Table 6.1.

6.2.3 Experimental Results

The Gulf of Mexico site includes both oil slicks related to the Deepwater Horizon accident and oil seeps. Test sites and corresponding radar and validation data sets selected for the generation of showcases are summarized in Table 6.2 and further described in the appendix.

In this sub-section the polarimetric approaches described in Sect. 6.2.2 are applied to actual polarimetric SAR data

Table 6.1 Expected behaviour of the polarimetric features

Polarimetric feature	Slick-free	Oil-covered
H	Low	High
A_{12}	High	Low
$\overline{\alpha}$	Low	Intermediate
NP	Low	High
μ	Positive	Negative
σ	Low	High

Table 6.2 Test sites and corresponding radar and validation data selected for the generation of showcases on oil at sea observation

Application/Product	Test site – radar data	Reference data
Oil at sea observation	Gulf of Mexico	Deepwater Horizon oil slick
	3 RADARSAT-2 fine quad-pol	
	Gulf of Mexico	Oil seeps
	2 RADARSAT-2 fine quad-pol	
	Gulf of Mexico	Deepwater Horizon oil slick
	1 UAVSAR MLC quad-pol	

where verified oil slicks are present to clearly show the added-value information that can be obtained by PolSAR data. All the polarimetric features provide similar results; hence, to save space, only the outputs obtained using NP and μ, evaluated over the whole image by using a 7×7 average moving, are shown.

The first experiment is relevant to the RADARSAT-2 SAR scene collected on May 15, 2010. The wind speed is 4–7 m/s, and the incidence angle varies in the range 29.1°–30.9°. The imaged scene contains few slicks, related to the Deepwater Horizon accident, that result in areas darker than the background sea both in the Pauli and in the single-polarization grey-tones VV image; see Fig. 6.1a, b. There are also few bright spots that are due to metallic targets at sea. It can be noted that the slick-covered sea area is very heterogeneous and presents some holes that, although present also in the VV-polarized image, are better visible in the Pauli image.

The outputs of *NP* and μ are shown in Fig. 6.1c, d. The *NP* image [see Fig. 6.1c] clearly shows the slick-covered areas that result in *NP* values larger than the background sea. Note that also metallic targets result in lager *NP* values. A deeper analysis on *NP* values reveals that slick-free and slick-covered sea surface is not well-separated. NP results in very low values both for slick-free and slick-covered sea surface ($NP < 0.1$). This clearly witnesses that the amount of unpolarized backscattered energy is very low over the whole scene. In electromagnetic terms, this witnesses that the dominant scattering mechanism over the whole scene (with the exception of the metallic targets) is the Bragg/tilted-Bragg mechanism. This result agrees to the conclusions drawn in Minchew et al. (2012) and Migliaccio and Nunziata (2014)), where UAVSAR data related to the Deepwater Horizon accident were processed. From a physical viewpoint, this unconventional result can be explained considering that (a) the oil released by the Deepwater Horizon was a "light oil"; (b) a massive use of dispersant was made that generated a mixture oil/water/chemical dispersants that cannot still considered oil; and (c) the spill occurred in a very different way if compared to "conventional" accidents or illegal discharges, since the oil came from the bottom of the sea. With respect to μ [see Fig. 6.1d], it is worth noting that it calls for positive values everywhere, witnessing that Bragg scattering dominates the whole scene.

This experiment clearly shows the extra benefit provided by polarimetric SAR data for oil at sea observation. PolSAR data result in an unprecedented amount of information that can be used to infer detailed information on the scattering mechanism of the observed scene. This information can be related, at least in a rough way, to the damping properties of

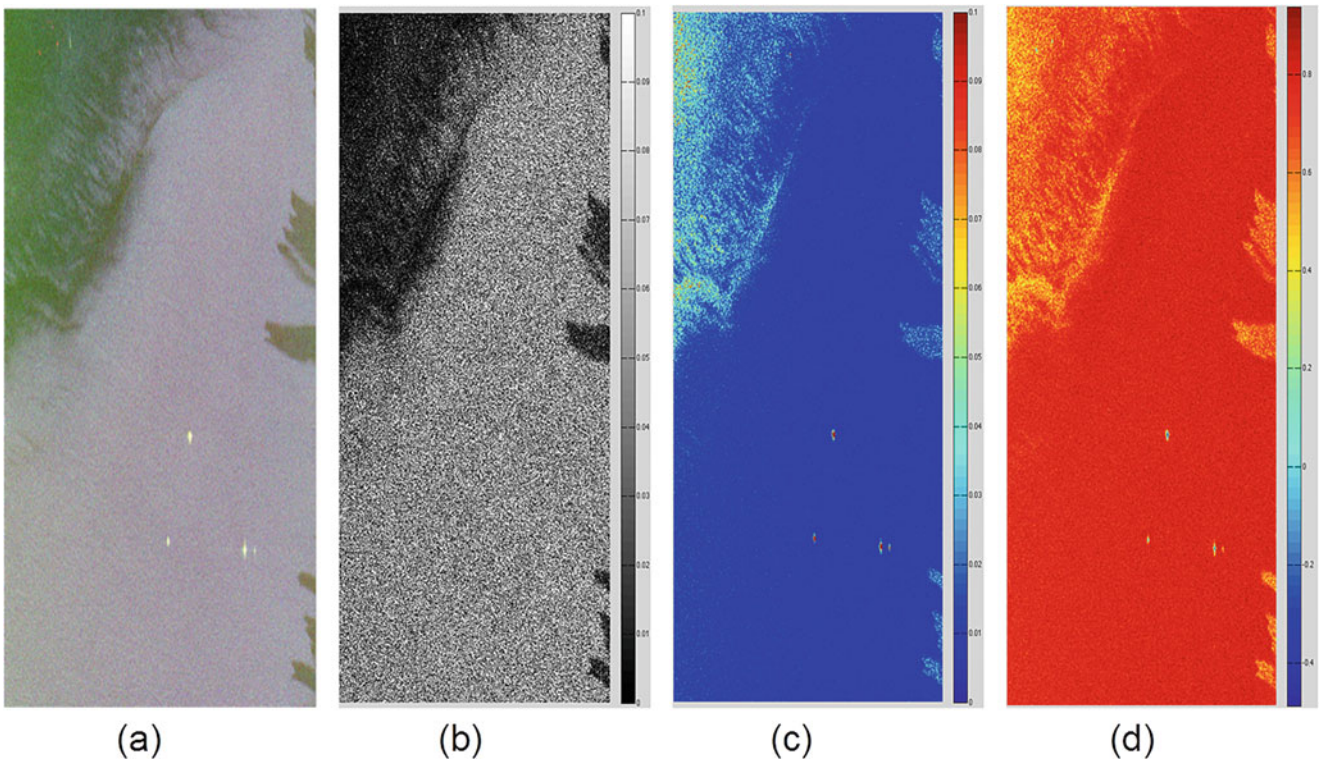

Fig. 6.1 RADARSAT-2 SAR data collected on May 15, 2010 over the Gulf of Mexico. (**a**) Pauli image. (**b**) Squared-modulus VV-polarized SAR data. Outputs of the *NP* (**c**) and μ (**d**) approaches

the oil slick or to the kind of surfactant that is present. It must be explicitly pointed out that this information cannot be extracted from single-polarization intensity SAR data.

The second experiment is relevant to the RADARSAT-2 SAR scene collected on May 8, 2010. The wind speed is 6 m/s, and the incidence angle varies in the range 41.9°–43.3°. The imaged scene contains few slicks, related to a well-known oil seep in the Gulf of Mexico. Those slicks result in "green" areas in the Pauli image and in areas darker than the background sea in the single-polarization grey-tones VV image; see Fig. 6.2a, b.

The outputs of the *NP* and μ approach are shown in Fig. 6.3a, b, respectively. It can be noted that, unlike the previous experiment, in this case, all the polarimetric approaches result in good separation between oil-covered and slick-free sea surface. From an electromagnetic viewpoint, one can say that this scene is everywhere dominated by Bragg scattering but within the oil-covered sea surface. With respect to NP, it can be noted that oil-covered sea surface results in a significant amount of unpolarized backscattered energy ($NP > 0.5$), which is compatible with a non-Bragg scattering mechanism, while a significantly lower unpolarized energy applies in case of slick-free sea surface. It can be also noted that μ results in positive (negative) values over slick-free (oil-covered) sea surface, allowing a clear and unambiguous distinction between the two scattering mechanisms.

Since in this case a "conventional" oil slick is in place, it is worth analysing the performance of the polarimetric features in terms of the detection capability. Within this context, the most attractive polarimetric feature is the conformity coefficient (or, equivalently, the approach proposed in Nunziata et al. (2008))), since it is able to separate in two non-overlapped regions: Bragg and non-Bragg scatterings without any external threshold. The logical true (sea) and false (oil) output obtained using μ is shown in Fig. 6.3c. As expected, positive (true) μ values result from sea surface Bragg scattering, while negative (false) μ values result from the oil-covered sea surface non-Bragg scattering. It must be explicitly pointed out that no empirical threshold must be set, and this is a key advantage of PolSAR approaches with respect to single-polarization ones.

These results demonstrate the unique benefit of PolSAR data for oil at sea observation with respect to single-polarization SAR data. In fact, polarimetric data result in unprecedented information that in no way can be extracted from single-polarization intensity data.

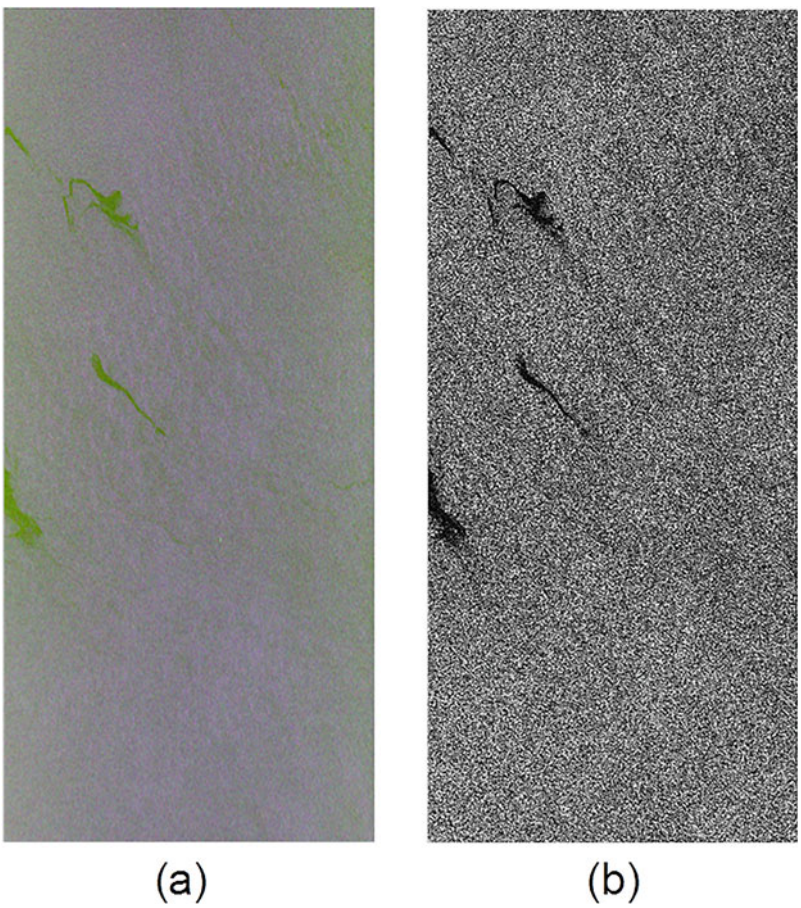

Fig. 6.2 RADARSAT-2 SAR data collected on May 8, 2010 over the Gulf of Mexico. (**a**) Pauli image. (**b**) Squared-modulus VV-polarized SAR data

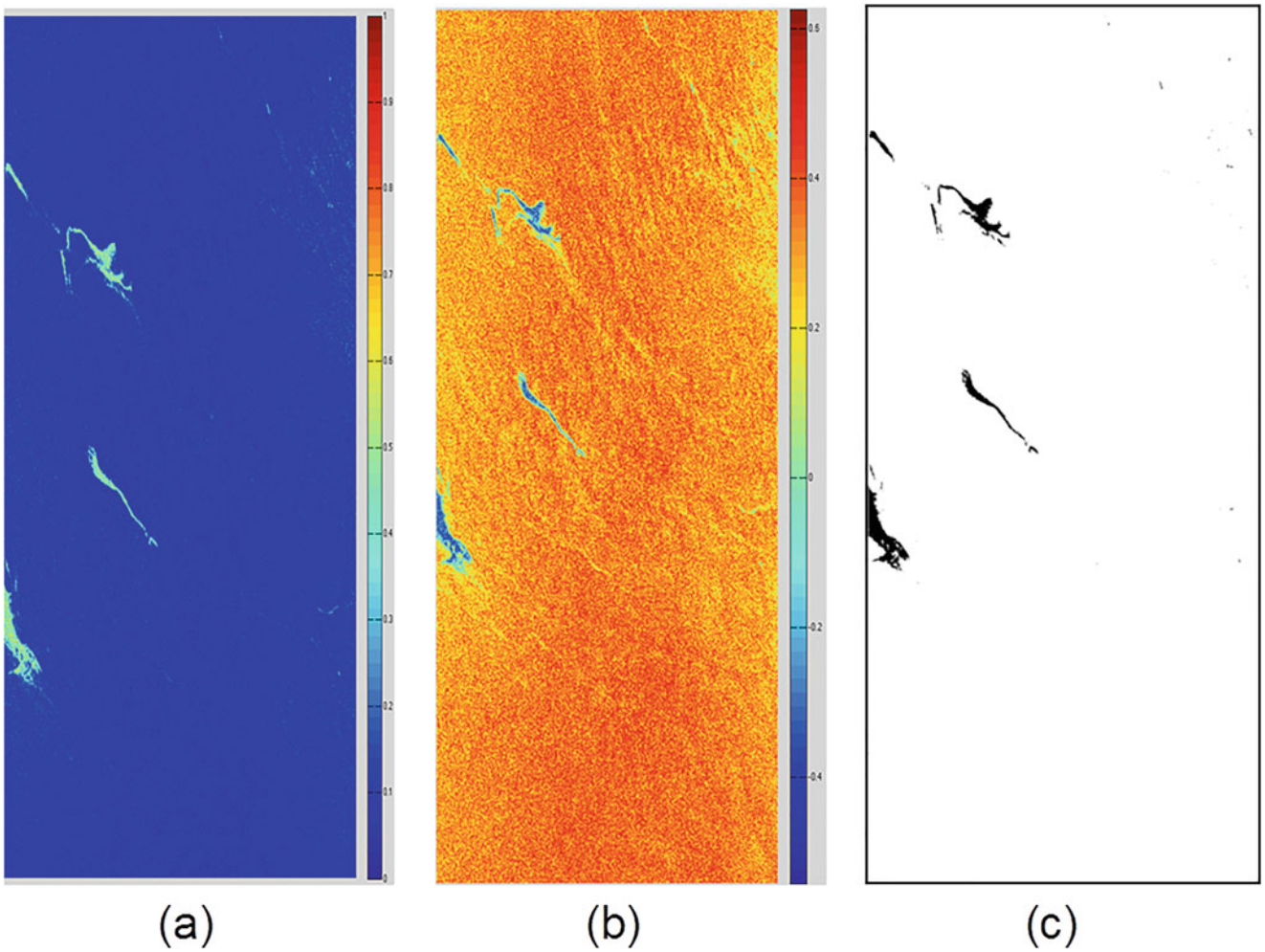

Fig. 6.3 Output of the *NP* (**a**) and μ (**b**) approach, binary μ image (**c**)

6.2.4 Comparison with Single/Dual Polarization Data

In this sub-section the dual-polarimetric σ approach is verified against actual polarimetric SAR data to discuss its performance with the above-described quad-polarimetric approaches. Note again that σ is the standard deviation of the co-polarized phase difference.

The output of the σ approach applied to the RADARSAT-2 SAR scenes of Figs. 6.1, and 6.2 is shown in Fig. 6.4a, b, respectively. The slick-covered areas are emphasized by the σ approach, as expected. With respect to Fig. 6.4a, the mean σ value related to slick-free and slick-covered sea surface is 30° and 45°, respectively. Hence, as far as for the quad-polarimetric approaches, the scattering mechanism that characterizes slick-covered sea surface is compatible with a Bragg mechanism. With respect to Fig. 6.4b, even in this case, the σ approach provides results similar to the quad-polarimetric ones. The output witnesses that a highly non-Bragg scattering mechanism characterizes the oil-covered sea surface, resulting in larger σ values (~110°). A different scattering mechanism characterizes the surrounding sea, where the mean σ value is ~55°. Even in this case, as far as for the quad-polarimetric approaches, σ values larger than expected are measured over sea surface that results to be very heterogeneous in terms of σ values, showing that, probably, a larger oil-affected area is present. Moreover, the area that surrounds the slicks is characterized by intermediate σ values, witnessing that low oil concentration/mixing phenomena apply.

6.2.5 Discussion on the Role of Polarization, on the Maturity of the Application and Conclusions

Experiments clearly witness that the extra information inherently carried on polarimetric SAR data allows not only detecting oil at sea but also (and often more importantly) to provide a rough information on the kind of surfactant and on

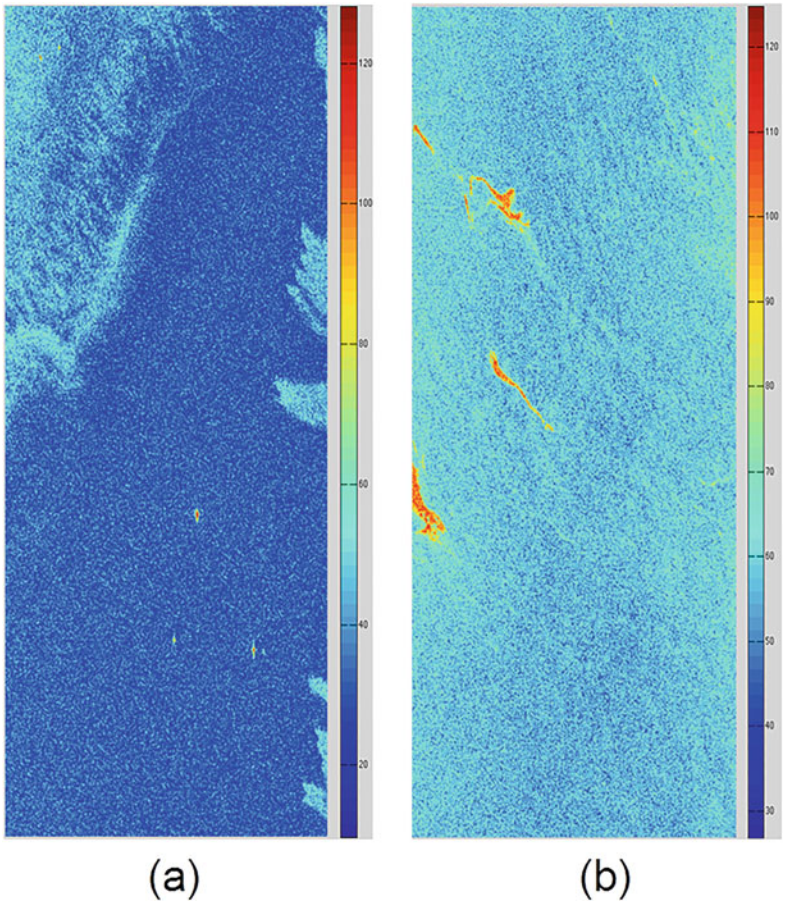

Fig. 6.4 $-\sigma$ [°] map related to the RADARSAT-2 SAR scene of Figs. 6.1 (**a**) and 6.2 (**b**)

its damping properties. Hence, SAR polarimetry is able to offer an unprecedented level of scattering details that can be used to assist classical "large swath" single-polarization procedure providing extra information on the surfactant. The application is mature: the proposed techniques have been successfully verified against actual polarimetric L-, C- and X-band SAR data collected in a broad range of incidence angles and sea state conditions.

6.3 Targets at Sea Observation

6.3.1 Introduction, Motivation and Literature Review

Sea metallic targets, i.e. oil rigs and ships, observation is nowadays a topic of great applicative interest. Both traffic-related and surveillance applications need a synoptic, all-weather and day and night observation system. The SAR is the key remote sensing tool for this application. However, SAR metallic targets observation is not an easy task. Specifically, one of the main issues to be tackled is the presence of false alarms versus missed targets.

In this section, the benefits of using fully polarimetric SAR data for targets at sea observation are carefully analysed. Accordingly, the most up-to-date state-of-the-art detectors able to deal with full- and dual-polarimetric single look complex (SLC) SAR data are briefly reviewed, and their performance is analysed using actual full-polarimetric SAR data collected in selected test sites. Then, a fair intercomparison of the detectors is accomplished in order to clearly show the benefits related to the use of fully polarimetric SAR data. As a benchmark, a single-polarization HV detector, based on the generalized-K (GK) distribution, is also applied to the HV SLC SAR data to clearly point out the benefits of radar polarimetry for targets at sea observation.

Metallic targets, being characterized by structures large with respect to the electromagnetic wavelength, call for a backscatter signal stronger than the background sea. Hence, they appear as bright spots in the SAR image plane. Following this rationale, several radiometric-based approaches have been developed to observe targets in single-polarization SAR data (Crisp 2004). However, the information provided by the backscattered intensity collected by a single-polarization SAR is not always sufficient to effectively observe metallic targets. To conceive more effective observation techniques,

great attention to polarimetric approaches has been paid. In fact, new high-performance polarimetric SARs, e.g. the ones operated onboard the Advanced Land Observing Satellite-2 (ALOS-2), RADARSAT-2, TerraSAR-X and COSMO-SkyMed missions, are of particular interest.

In Liu et al. (2005)), a ship detector, that applies a likelihood ratio test with the Neyman-Pearson criterion to define a pixel-based detection criterion, is developed. Gaussian distributions for the scattering matrix components were assumed in order to derive an approximate decision variable. Even though the Gaussian distribution does not fit perfectly the data, the test shows good accuracy on real data. In Yeremy et al. (2001)), two studies have been accomplished using airborne C-band polarimetric SAR data. The first study compares target-to-clutter ratios (TCRs) for various polarimetric channels, demonstrating that the best polarimetric channel for ship observation purposes depends on the incidence angle. Co-polarized horizontal channel (HH) performs better than cross-polarized one (HV) for larger incidence angles. Moreover, a comparative study on the suitability of two polarimetric target decomposition techniques, i.e., the coherent target decomposition (CTD) and Van Zyl decomposition (VZD), is also undertaken, demonstrating that CTD performs better than VZD in terms of false alarm rate. In Touzi and Charbonneau (2002)), the CTD is enhanced to extend its range of applicability, and the symmetric scattering characterization method (SSCM) is introduced to better exploit the information provided by the symmetric scattering component in the frame of coherent scattering. In Ferrara et al. (2011)), a speckle-based multi-polarization study is developed to define a physically based single-polarization filter. It is shown that a proper combination of speckle-related parameters, when evaluated over the cross-polarized channel, is able to observe targets at sea with a very low false alarm rate. In Novak et al. (1989)), a linear polarimetric detector that maximizes the target-to-clutter contrast, the so-called polarimetric matched filter (PMF), is derived, and the structure of this detector is related to simple polarimetric targets types.

These approaches are meant to identify a set of polarimetric features peculiar to the metallic targets (e.g. high polarimetric entropy, large coherent component, etc.), but, unfortunately, there is a strong dependence on the scattering mechanism of both target and surrounding background. A different approach is proposed in Marino (2013)) where a notch filter for target detection purposes is developed. Experiments on C-band RADARSAT-2 full-polarimetric SAR data demonstrate the capability of the approach to highlight features, which are polarimetrically different from the background sea in a broad range of sea state conditions and almost independently of look angle. In Nunziata et al. (2012b)), a polarimetric detector that exploits the different symmetry properties that characterize sea surface with and without metallic targets is proposed. The detector works on dual-polarimetric HH/HV (VV/VH) pairs, and it exploits the cross-correlation between co- and cross-polarized channels to detect targets at sea in a robust and effective way. Experiments accomplished using L-band ALOS-PALSAR, C-band RADARSAT-2 and X-band TerraSAR-X data confirmed the effectiveness of the proposed approach. In Nunziata and Migliaccio (2013)), X-band dual-polarization Cosmo-SkyMed PingPong SAR data are exploited to observe metallic targets at sea in a very effective way.

6.3.2 Methodology

In this section the operational procedures used are briefly described, starting from quad- and dual-polarimetric detectors, and, finally, a single-pol detector is considered as a benchmark.

6.3.2.1 Liu Et al. Detector

The detector is fully described in Liu et al. (2005)). It assumes that ocean and target backscatter follow a zero-mean multivariate Gaussian distribution; hence, a likelihood ratio test is proposed, based on the Neyman-Pearson criterion to maximize the detection probability subject to the constraints that the probability of false alarm is less than a prefixed value. Moreover, typically the elements of covariance matrix of the target, $\mathbf{C}_t$, are much larger than the ones related to the sea, $\mathbf{C}_0$; hence, a simplified decision rule can be used:

$$\Lambda = \mathbf{k}^* \mathbf{C}_o^{-1} \mathbf{k} = \begin{cases} > T_l & \text{target} \\ \leq T_l & \text{ocean} \end{cases} \tag{6.1}$$

where $\mathbf{k}$ is the target scattering vector. This detector is sub-optimal; the magnitude of the measured data over sea surface typically does not strictly follow a Gaussian distribution, showing significant tails. In the following the value of probability of false alarm used for setting the threshold is $P_f = 10^{-5}$.

6.3.2.2 Geometrical Perturbation Polarimetric Notch Filter

This ship detector shares the same general methodology of the geometrical perturbation partial-target detector (GP-PTD), and physical justification of the algorithm can be found in Marino (2013)). The idea behind the GP-PNF is to build an algorithm that is able to identify any partial target, which is different from the background clutter. In the case of ship detection, the background is the sea. Hence, the following decision rule is proposed (Marino 2013):

$$\gamma_n = \frac{1}{\sqrt{1 + \frac{RedR}{\mathbf{t}^{*T}\mathbf{t} - \left|\mathbf{t}^{*T}\widehat{\mathbf{t}}_{sea}\right|^2}}} > T_n \tag{6.2}$$

where $\mathbf{t}$ is the partial vector extracted from the scene (observables), T_n is the threshold, and *RedR* is a detector parameter that can be set using a rationale based on the signal-to-clutter ratio (SCR) [R17]. The solution followed in this report is to set the threshold to $T_n = 0.98$ and choose *RedR* based on the intensity of the minimum target of interest P_T^{min}. In this study P_T^{min} is about 0.2 (linear scale).

6.3.2.3 Polarimetric Match Filter

This detector was firstly introduced in Novak et al. (1989)), and it considers an optimization of the power ratio between the quadratic forms of the covariance matrices of target and clutter. The optimization is easily carried out exploiting the Lagrangian method:

$$\begin{aligned} L =& \boldsymbol{\omega}^{*T}\mathbf{T}_{sea}\boldsymbol{\omega} - \lambda\left(\boldsymbol{\omega}^{*T}\mathbf{T}_t\boldsymbol{\omega} - C\right) \\ \Rightarrow& \frac{\partial L}{\partial \boldsymbol{\omega}^{*T}} = \mathbf{T}_{sea}\boldsymbol{\omega} - \lambda\mathbf{T}_t\boldsymbol{\omega} = 0 \Rightarrow \mathbf{T}_{sea}^{-1}\mathbf{T}_t\boldsymbol{\omega} = \lambda\boldsymbol{\omega} \end{aligned} \tag{6.3}$$

The latter says that the optimum scattering mechanisms $\boldsymbol{\omega}$ are the ones that diagonalize the matrix $\mathbf{A} = {\mathbf{T}_{sea}}^{-1}\mathbf{T}_t$. Even though $\mathbf{A}$ is not Hermitian, it can be proved that it admits real positive eigenvalues. The maximum eigenvalue represents the maximum contrast; therefore the detector is finalized in setting a threshold on this. In this report a value of contrast equal to 9 is considered.

6.3.2.4 Reflection Symmetry Detector

In this sub-section the theoretical rationale that lies at the basis of the polarimetric detector (Nunziata et al. 2012b) is briefly outlined. The underpinning idea is that natural distributed targets (sea surface) satisfy reflection symmetry, while man-made metallic targets call for larger departure from this condition. To highlight the different target/sea behaviour in dual-polarized SAR data, the modulus of the correlation between like- and cross-polarized scattering amplitudes is used (Nunziata et al. 2012b):

$$X = \left|\left\langle S_{hh}S_{hv}^{*}\right\rangle\right| > T \tag{6.4}$$

To obtain a binary mask, a threshold T is used. Here, $T = 0.04$ is used.

6.3.2.5 GK Filter

In this sub-section the single-polarization detector proposed in Ferrara et al. (2011)) is briefly outlined. An electromagnetic model, based on the generalized-K (GK) distribution, is proposed in Ferrara et al. (2011)) that allow observing the scattering features associated with metallic targets at sea in full-resolution single-look-complex (SLC) SAR data. Hence, a simple and effective approach to observe targets at sea in HV-polarized SLC SAR data is proposed. In Ferrara et al. (2011)), the following index is shown:

$$\gamma = \left(\frac{1}{2\eta}\right)^2 \tag{6.5}$$

where η is related to the rice factor (Ferrara et al. 2011) and, when evaluated over the HV channel, is able to sort targets and sea areas in two nonoverlapping sets, i.e. $\gamma < 1$ and $\gamma > 1$, respectively. Following this theoretical rationale, a simple filter that implements (6.5) is developed that operates on SLC SAR data using two nested windows, to estimate the coherent and incoherent backscattered field components, whose sizes are 8×8 and 18×18, respectively.

6.3.3 Experimental Results

Test sites and corresponding radar and validation data sets selected for the generation of showcases on targets at sea observation are summarized in Table 6.3 and further described in the appendix.

In this sub-section the full-polarimetric detectors, i.e. Liu et al., geometrical perturbation-polarimetric notch filter (GP-PNF) and the polarimetric match filter (PMF), are verified against actual polarimetric RADARSAT-2 SAR data (see Sect. 6.3.2).

One meaningful experiment, relevant to the scene collected on May 15, 2010, is detailed. The scene consists of six targets: one oil rig and five visually inspected targets. The Pauli image and the HH-polarized squared-modulus SAR data are shown in Fig. 6.5a, b, respectively. The location of the targets was derived by a map (i.e. ground truth), and it is shown as red boxes in the image. Moreover, a visual inspection of the radar image was carried out trying to interpret the points in the image that may represent vessels. The latter are marked by yellow circles.

Table 6.3 Test sites and corresponding radar and validation data selected for the generation of showcases on targets at sea observation

Application/Product	Test site – radar data	Reference data
Targets at sea observation	Gulf of Mexico	Oil/gas rigs/platform Google Earth map
	3 RADARSAT-2 fine quad-pol	

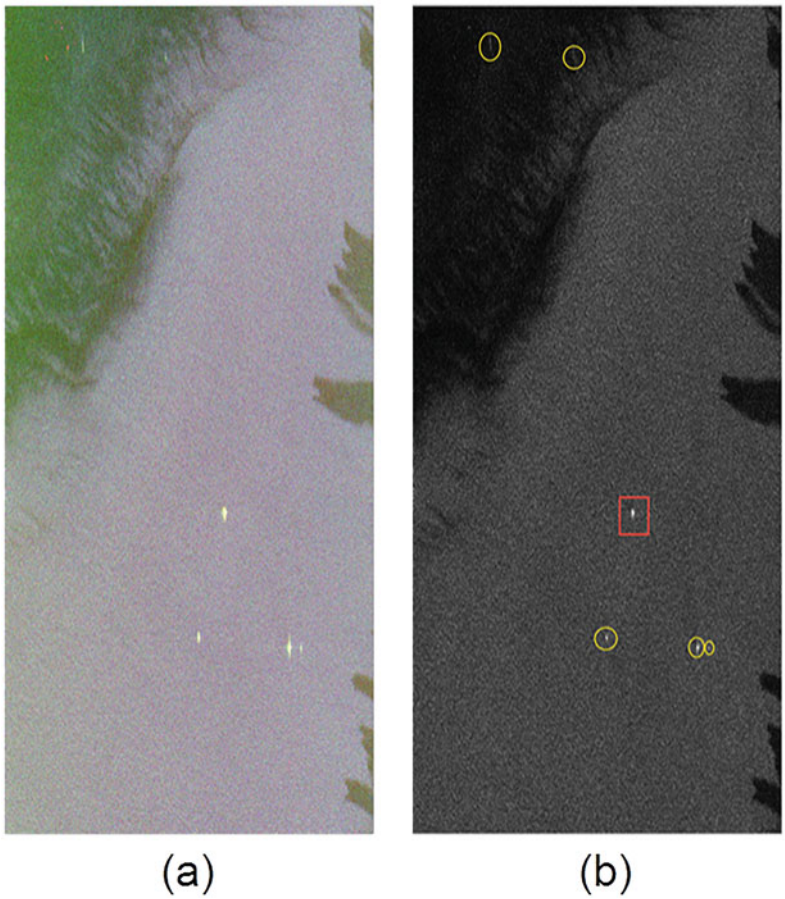

Fig. 6.5 RADARSAT-2 SAR data collected on May 15, 2010, over the Gulf of Mexico. (**a**) Pauli image. (**b**) Squared-modulus HH-polarized SAR data. Yellow circles, visually inspected vessels; red boxes, verified metallic targets. Dark areas are related to the oil spilled during the Deepwater Horizon accident

The output of the full-polarimetric Liu et al., GP-PNF and PMF detectors is shown in Fig. 6.6a, c, respectively. The detection masks show that all the targets identified in the scene are detected. Moreover, all the quad-polarimetric detectors seem to detect two points in the upper left corner. These appear in the Pauli image [see Fig. 6.5a] as bright red spots, and, hence, they can be associated to dihedral structures. It is not clear what the points are since their brightness is relatively low (therefore we did not consider them belonging to vessels in the visual inspection). However, their polarimetric behaviour is particularly well-defined (and repeated among them), and therefore we do not believe that they are common false alarms. It may be speculated that they are small vessels or probes beside the larger vessel or just ambiguities/artefacts. In the absence of accurate ground measurements, it is not possible to provide any specific conclusion. Finally, the PMF seems to be particularly sensitive to changes of the polarimetric background, and it is able to detect one of the ambiguities in the image that appears very faint in the Pauli RGB. This is clearly not a genuine target; however, it is an illustration of the power of these algorithms in picking up anomalies on the background. In general, azimuth ambiguities can be somehow filtered out by some algorithms; therefore it should be possible to remove this typology of false alarms with some post-processing. In general, more tests should be carried out in order to understand if the PMF high sensitivity may constitute a drawback in practical application (i.e. leading to irremovable false alarms).

6.3.4 Comparison with Single/Dual Polarization Data

In this sub-section the dual-polarimetric symmetry detector and the single-polarization (HV) GK filter are verified against actual polarimetric RADARSAT-2 SAR data.

The symmetry detector and the GK filter outputs obtained processing the SAR scene of Fig. 6.5 are shown in Fig. 6.7a, b, respectively.

The symmetry detector succeeds in observing all the targets highlighted in Fig. 6.5b. The two "potential" targets observed by all the quad-pol detectors are not present in the symmetry output. The single-polarization detector misses one target (the one on the upper left side of the image). Moreover, even this detector does not observe the two "potential" targets. These results clearly witness the superiority of polarimetric detectors with respect to the single-polarization HV one.

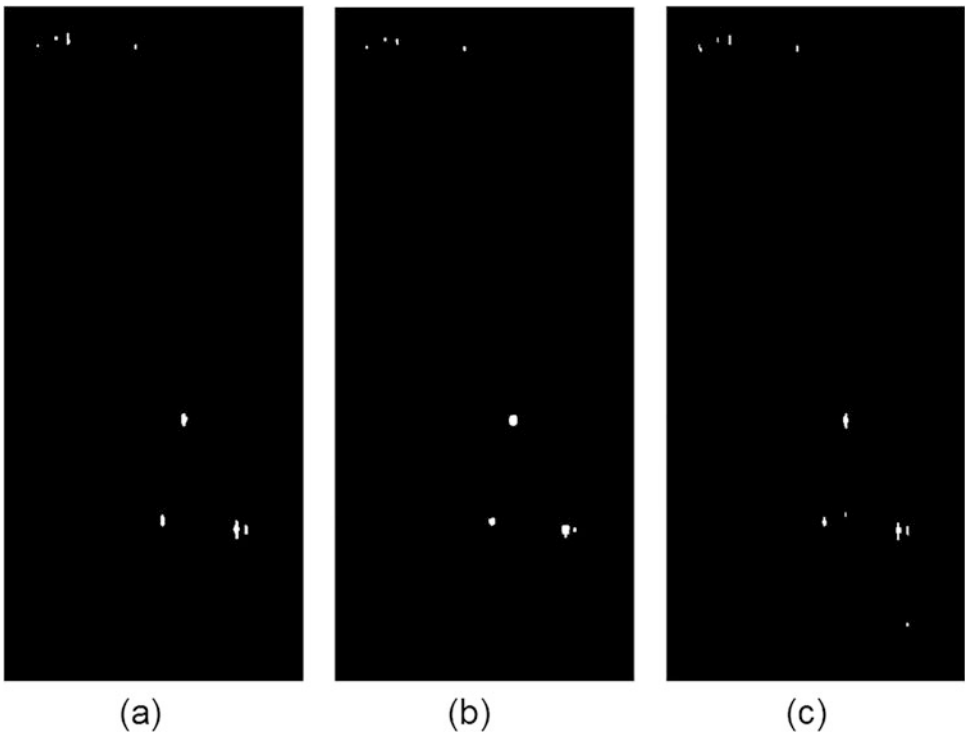

Fig. 6.6 Output of the full-polarimetric detectors. (**a**) Liu et al., (**b**) GP-PNF, (**c**) PMF

6.3.5 Discussion on the Role of the Polarization, on the Maturity of the Application and Conclusions

In this section, some of the most up-to-date polarimetric detectors to observe metallic targets at sea in PolSAR images are reviewed, and their performance is discussed using actual RADARSAT-2 SAR data where both visually inspected and verified targets are present.

Experimental results clearly witness that the extra information inherently carried on polarimetric detectors allows a better discrimination of the "anomalies" in the polarimetric backscattering of sea surface related to targets. This results in a better target/sea discrimination, even when very challenging scenes are considered, e.g. the one showed in Fig. 6.5, where few targets are present within a low backscatter area. Hence, SAR polarimetry is able to offer an unprecedented level of scattering details that can be used to detect targets that cannot be observed when using conventional single-polarization detectors. On this purpose, it must be explicitly noted that some of the "potential" targets detected only by the quad-pol detectors are very complicated to be visually inspected from the HH or HV SAR image. Hence, if confirmed they would clearly witness the benefits of quad-pol detectors in detecting even targets characterized by low signal-to-noise (SNR) ratio. These results pushed toward a fair intercomparison of the above-mentioned approaches using a SAR data set where verified small targets are present (see external contributor document).

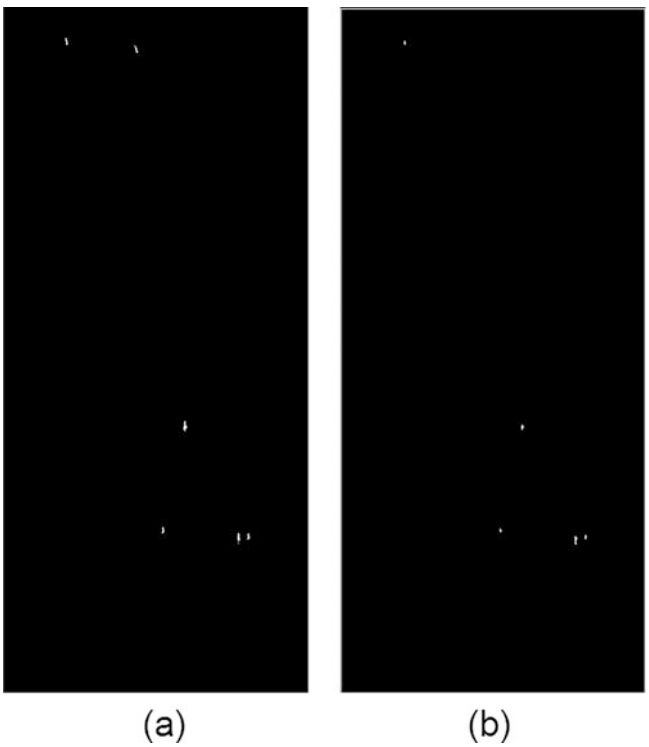

Fig. 6.7 RADARSAT-2 SAR scene of Fig. 6.5. (**a**) Dual-polarimetric symmetry detector output. (**b**) Single-polarization HV GK filter output

The application is mature: the proposed techniques have been successfully verified against actual polarimetric L-, C- and X-band SAR data collected in a broad range of incidence angles and sea state conditions.

6.4 Polarimetric Synthetic Aperture Radar Measurements of Oil Pollution at Sea

6.4.1 Introduction, Motivation and Literature Review

Full-polarimetric SAR systems allow us to link scattering processes and variations in the backscattered signal to the physics of the medium measured. Recent advances in the field show a potential in polarimetric SAR measurements with respect to discrimination between different types of oil or surfactants and in deriving valuable information about oil slicks physical properties. In this showcase, we demonstrate that multi-polarization SAR can be used to obtain key information for pollution response authorities about detected slicks at sea (Skrunes et al. 2015).

The experimental work described in this chapter has been conducted by University of Tromsø in collaboration with Norwegian Clean Seas Association for Operating Companies (NOFO), with funding from Total E & P Norge AS and the Norwegian Space Centre (NSC).

Occasionally, large amounts of oil are spilled into the sea. The Deepwater Horizon accident in the Gulf of Mexico in 2010 and the Prestige accident off the coast of Galicia in 2002 are examples of such incidents. During the recovery and cleanup phase, information about slick properties, such as the thickness distribution and the oil volume fraction, is requested. Deliberate man-made slicks are often smaller in size but are nevertheless frequently occurring. Biogenic slicks and natural seeps are also known to resemble oil spills in mono-polarization SAR imagery. Therefore, knowledge about the slick type and its origin is useful input to decision-makers. This type of information could limit the number of false alarms as well as expensive actions taken by authorities.

Hence, beyond simply detecting the slicks, a demand for additional information is recognized. This has triggered the scientific community to explore polarimetric SAR systems and their potential in:

- Discriminating man-made mineral slick types from mono-molecular biogenic slicks and
- Characterizing slicks, e.g. to obtain knowledge on slick thickness and infer oil/water mixing

The ocean is a nonstationary medium, and oil slicks are affected by weathering processes over time. Weathering processes include spreading, drift, evaporation, dissolution, natural dispersion, emulsification, sedimentation, biodegradation and photooxidation (Kotova et al. 1998). This can cause significant variability in the signatures of oil pollutants in SAR imagery. The detection and characterization capabilities of SAR systems also show a dependence on imaging geometry and SAR system properties, e.g. incidence angles and sensor frequency. Norway is one of the few countries allowing oil discharges for the purpose of equipment and procedure testing. To gain increased knowledge in the field of oil spill remote sensing by SAR, controlled large-scale oil-on-water experiments are currently conducted in the North Sea. These experiments are excellent opportunities to create realistic study cases while having access to key parameters such as the oil types released, meteorological conditions and the age of the spills. This chapter describes the lesson learned from the Norwegian oil-on-water experiments in 2011 and 2012, seen from a polarimetric SAR remote sensing perspective.

For polarimetric SAR systems, when Bragg scattering is dominant, the cross-polarization term could be considered negligible. This assumption is made in the Freeman-Durden decomposition, where the first component models an untilted and slightly rough first-order Bragg surface. In the context of marine slicks, the strength of polarimetric SAR systems seems indeed to lie in the relation between the co-polarization coefficients (VV and HH) of the scattering matrix. The standard deviation of the co-polarized phase difference (CPD) is described as an important feature, which adds discrimination power to the problem of distinguishing oil spills from biogenic look-alikes (Migliaccio et al. 2009b). The co-polarization ratio is another feature that is sensitive to the dielectric properties of the surface (Minchew et al. 2012), and its potential is currently investigated with respect to discriminating oil from look-alikes in the marginal ice zone (Brekke et al. 2014). Solberg recently gave a literature review on remote sensing of oil pollution, where a brief summary of SAR and some additional polarimetric descriptors is included (Solberg 2012).

6.4.2 Methodology

6.4.2.1 Oil-on-Water Experiments

The NOFO conducts an oil-on-water exercise once a year in the North Sea. The purpose of these exercises is to improve the national oil spill preparedness. In 2011 and in 2012, the controlled discharges at sea provided a unique opportunity to acquire satellite data of various oil types and collect other auxiliary information about the oil spills. The substances were released from ships involved in the exercises, and SAR data was collected from European, American, Canadian and Indian satellites. Meteorological conditions were logged, and other data such as photos and infra-red

(IR) measurements were collected from vessels, aerostats and aircrafts.

6.4.2.2 Releases of Mineral and Biogenic Oil Types into the Sea Water

Kotova et al. (Kotova et al. 1998) emphasizes the importance of weathering processes, as they influence oil spills physico-chemical properties and detectability in SAR images. The processes that play the most important role for oil spill detection are evaporation, emulsification and dispersion. Lighter components of the oil will evaporate to the atmosphere. The rate of evaporation is dependent on oil type, thickness of the spill, wind speed and sea temperature. Emulsification of crude oil (crude oil is a naturally occurring substance and has been extracted, but no further processing is done) refers to the process where water droplets become incorporated in the oil and are estimated based on water uptake as a function of the wind exposure of the actual oil type. Dispersion is an important factor in deciding the lifetime of an oil spill, and it is strongly dependent on the sea state. While evaporation, dispersion and dissolution make the oil on the surface disappear, emulsification of the oil increase the viscosity and volume of the pollutant and promote its persistence (Reed et al. 1999). In the oil-on-water experiments taking place at the Frigg field, we have released both crude oil and water-in-oil emulsion to create realistic mineral oil slicks. Figure 6.8 shows crude (Balder) oil forming into a large slick on the ocean surface in 2011.

One look-alike phenomenon frequently discussed in the literature is natural biogenic slicks. Biogenic slicks are surface films consisting of surface-active compounds, originating from marine plants or animals. The main producers of natural surface films are algae and some bacteria. Surface-active organic compounds have one hydrophobic part and one hydrophilic part, i.e. strong tendencies both towards and against water. Hence, the molecules are spontaneously arranged at the air-water interface with the hydrophobic part up in the air and the hydrophilic part down in the water. This forms a very thin and so-called monomolecular film, which is only one molecule thick (~ 2.4–2.7 nm). In contrast, crude oil spills mainly consist of chemicals with exclusively hydrophobic character. Depending on the amount and viscosity of the oil and on the environmental conditions, crude oil spills will spread out over time. However, the final thickness still remains orders of magnitude larger than that of monomolecular films (μm, mm and even cm for freshly spilled oil) (Hühnerfuss 2006). The two slick types will have different viscoelastic properties and induce

Fig. 6.8 Left: The crude oil slick formed in June 2011. Vessels participating in the exercise are visible. (Photo: Kustbevakningen. Right: Release of palm oil ongoing at the Frigg field in 2011. Photo: Stine Skrunes)

different damping on the ocean waves (Hühnerfuss 2006). It is difficult to distinguish between mineral oil spills and natural slicks in mono-polarization SAR data. As a third substance applied in the oil-on-water experiments, we have chosen to use palm oil as a biogenic slick simulator. The palm oils viscoelastic behaviour is similar to the one of natural biogenic oil films. Figure 6.8 shows a photo of the release of 400 litres of palm oil in 2011.

6.4.2.3 Analysis of Multi-polarization SAR Data

The methodology applied in the analysis of the SAR datasets includes the following steps:

- Computation of multi-polarization features
- Masking of open sea water
- Unsupervised classification of the remaining slick pixels

The output from the classification is finally discussed in relation to the known in situ slick characteristics.

A quality investigation of SAR data recorded by Radarsat-2 and TerraSAR-X during the 2011 experiments has also been conducted. The analysis revealed that the signal over oil slicks in the cross-polarization channels (VH and HV) often fluctuates around the noise floor (Skrunes et al. 2012a). A threshold of −6 dB is proposed in Minchew et al. (2012)), where a study based on the airborne UAVSAR (L-band) system was undertaken. This requirement cannot be met by current spaceborne systems, such as Radarsat-2 and TerraSAR-X, as the signal level in the cross-polarization channels is fairly low over marine slicks. Hence, for the remainder of this chapter, we limit our attention to the co-polarization scattering coefficients (VV and HH), which have a stronger signal-to-noise ratio.

A selected set of multi-polarization features is applied as input to the unsupervised classification procedure. The names of the features considered are presented in Table 6.4, while more detailed definitions can be found in Skrunes et al. (2015, 2012b). The features are either processed from the mean covariance matrix or from target decomposition theorems. Some of them are well-known multipurpose descriptors. Others are in the literature specifically proposed for oil slick studies. Several of the features were originally developed for the full scattering matrix case. To comply with the discussion on data quality above, these features are here adapted to dual-polarization (only involving the VV and HH scattering coefficients, respectively).

Table 6.4 Features applied in this study

#	Feature
1	Entropy H
2	Anisotropy A′
3	Mean scattering angle $\overline{\alpha}$
4	Covariance scaling factor μ
5	Co-polarization power ratio γ_{CO}
6	Standard deviation of co-polarized phase difference $\sigma_{\phi CO}$
7	Magnitude of co-polarization correlation coefficient ρ_{CO}
8	Real part of co-polarization correlation r_{CO}

6.4.3 Experimental Results

The selected test site is the Frigg field in the North Sea, northwest of Stavanger. SAR measurements of the oil slicks artificially created in 2011 and 2012 have been successfully collected from spaceborne sensors. An overview of some of the datasets is given in Table 6.5.

An investigation of the features presented in Table 6.4 shows a varying degree of separability between the slick-covered areas and the ambient clean sea. Figure 6.9 presents some of the features listed in Table 6.4, i.e. the entropy, the covariance scaling factor and the real part of the co-polarization correlation. The features are computed from one of the quad-polarimetric Radarsat-2 fine-resolution scene recorded in 2011 (see Table 6.5). We can see that some of these features exhibit clear differences within the plant oil slick as compared to values within the mineral oil slicks. Particular regions within individual slicks are also more pronounced than other regions of the same slick.

The intensity image, in the bottom part of Fig. 6.9, shows the VV channel with labels indicating the slick types. As we can see, all slicks are clearly visible despite fairly low-wind speed at the time of recording. The bottom right image shows an unsupervised classification of the three different oil slicks. The classification result indicates a potential for discrimination between mineral oil and biogenic slicks. We can also observe zones along the edges of the mineral slicks. This zoning may be related to changes in physical parameters, e.g. the thickness distribution of the oil. Aerial photos of the crude oil, taken approximately 1 h before the satellite passed, reveal internal thickness variations corresponding to the Bonn Agreement Oil Appearance Code (BAOAC) (Skrunes et al. 2012b; Areal-surveillance – Cooperation on aerial surveillance over the North Sea area. In: Bonn Agreement Counter Pollution Manual 2005). This supports our SAR-based observations.

6.4.4 Comparison with Single/Dual Polarization Data

The simplest type of SAR systems transmits on one polarization and receives on the same (like) polarization. Current operational oil slick monitoring services are mainly based on mono-polarization SAR products (VV or HH polarization). Both support vector machines (SVM) and Bayesian

Table 6.5 Test sites and corresponding radar and validation data selected for the generation of showcases on observation of oil pollution at sea

Sensor	Date and pass	Mode and pol.	Oil slicks
Radarsat-2	8 June 2011 descending	Fine quad-polarization	Emulsion and plant oil
TerraSAR-X	8 June 2011 descending	Strip map, HH and VV	Emulsion
TerraSAR-X	8 June 2011 ascending	Strip map, HH and VV	Emulsion, plant oil and crude oil
Radarsat-2	8 June 2011 ascending	Fine quad-polarization	Emulsion, plant oil and crude oil
Cosmo-SkyMed	14 June 2012 ascending	PingPong, HH and VV	Emulsion and oleyl alcohol (OLA) or plant oil
Cosmo-SkyMed	14 June 2012 descending	PingPong, HH and VV	Emulsion and plant oil
Radarsat-2	15 June 2012 descending	Fine quad-polarization	Emulsion and plant oil
TerraSAR-X	15 June 2012 ascending	Strip map, HH and VV	Emulsion
Radarsat-2	15 June 2012 ascending	Fine quad-polarization	Emulsion
Cosmo-SkyMed	15 June 2012 ascending	PingPong, HH and VV	Emulsion

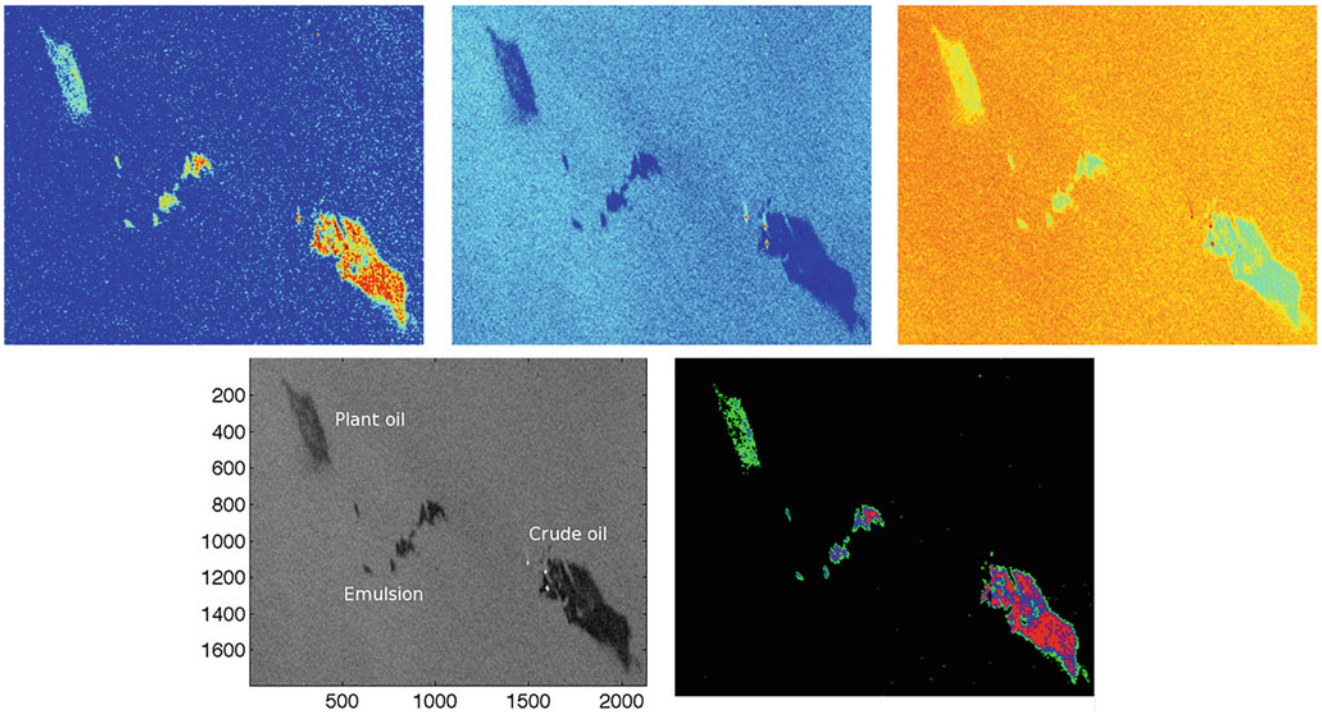

Fig. 6.9 Top row: entropy (left), covariance scaling factor (middle) and co-polarization correlation (right). Bottom row left: VV intensity image from June 2011 at a wind speed of 1–3 m/s. RADARSAT-2 data and products© MDA LTD. (2011) – All Rights Reserved. Bottom row right: an unsupervised K-means classification based on the set of multi-polarization features visualized in the top row. The open water is masked out (black)

classification schemes have previously been proposed for oil slick detection and oil spill versus look-alike discrimination based on Radarsat-2 ScanSAR or ENVISAT ASAR Wide Swath SAR scenes (Brekke and Solberg 2008). These algorithms are trained and tested on large data sets with reasonable good performance. However, it is shown that oil spills can be hard to separate from look-alikes when only utilizing mono-polarization SAR images. From the mono-polarization intensity or amplitude products, the information we can extract about the slicks are mainly related to the geometry and shape of the segmented region, properties of the backscatter level of the spot and the surroundings, spot contextual information and texture.

True polarimetric SAR modes are necessary to be able take advantage of the technology discussed in this chapter. Hence, the previous alternating polarization (AP) mode of ENVISAT or the current PingPong (PP) mode of Cosmo-SkyMed is not ideal for oil slick characterization. These modes suffer from a time lag between the transmissions of the horizontal and vertical polarized signals. The delay is long enough to cause an incoherent imaging over sea surfaces (Nunziata et al. 2011). These data products can simply be described as images, as they do not include the relative phase between the two received channels. Techniques applicable to these data types are primarily restricted to ratios or differences of their respective images.

With the launch of Advanced Land Observing Satellite (ALOS) in 2006 and TerraSAR-X and Radarsat-2 in 2007, coherent dual- and quad-polarimetric SAR measurements became available from space. The scattering matrix holds all the complex scattering coefficients that describe the marine target. The scattering coefficients are measured at different linear combinations of send and received polarizations (VV, HH, VH and HV). The polarimetric SAR systems extend our capabilities to characterize the slicks. It provides us with a mean to investigate the physical scattering characteristics of the surface medium. However, due to limitations in the current technology, only narrow swath modes are available.

In compact polarimetry, one polarization is transmitted, and two orthogonal polarizations are received, together with their relative phase. With this technique, one realizes some of the benefits of quad-polarimetric SAR systems, but not all. An advantage is an extended coverage. However, with compact polarimetry one only gets access to a 2 × 2 coherency matrix, whereas quad-polarimetric systems measure the covariance matrix (Raney 2011). Compact polarimetry for oil slick detection has been investigated by simulating compact polarization from Radarsat-2 quad-polarimetric SAR data (Salberg et al. 2012; Shirvany et al. 2012; Nunziata et al. 2015).

6.4.5 Discussion on the Role of Polarization, on the Maturity of the Application and Conclusions

We conclude that polarimetric SAR measurements have an improved ability to discriminate between mineral oil slicks and look-alike phenomena, as well as a potential for slick characterization. Interesting internal slick variations are observed, which may be related to differences in thickness or oil volume fraction.

However, we would like to emphasize that, beyond simply detection, a sufficiently high signal-to-noise ratio is necessary to succeed in any physicochemical slick information extraction by polarimetric SAR. Currently, only the VV and HH channels from satellites such as Radarsat-2 and TerraSAR-X can be utilized for oil slick characterization, while some airborne sensors (e.g. the UAVSAR) have a low enough noise floor to allow exploitation of the whole scattering matrix, which also includes the cross-polarization channels. We would therefore like to emphasize that the choice of SAR sensor properties, such as the noise floor level and the selection of incidence angles, needs to be carefully considered when designing new missions aiming for oil pollution monitoring.

To lift the application described in this chapter to an operational stage, our aim is first to test the techniques on a wider range of data samples, including a wider spectre of metrological conditions, water-in-oil mixtures and surfactants, and second to build up a training dataset that could be used as input to a supervised classifier.

6.5 Ship Detection

6.5.1 Methodology

The aim of this section is to present a comparison of ship detectors exploiting quad-, dual- and single-polarimetric data over a dataset where a ground survey was carried out during the acquisition. A theoretical presentation of the algorithms exploited for ship detection is included in the previous sections and introductory chapters.

6.5.2 Test Sites and Data Sets

Test sites and corresponding radar and validation data sets selected for the generation of showcases on ship detection are summarized in Table 6.6.

6.5.2.1 Brief Polarimetric Analysis of the Data

All the algorithms consider an initial multi-look of 1 × 5 (range x azimuth) pixels applied on the elements of the covariance matrix. This makes the pixel more squared on the ground. Subsequently, a boxcar filter of 3 × 3 pixels is employed to further reduce the pixels statistical variation. Clearly, the samples are not all independent each other, and the equivalent number of looks (ENL) returned by such averaging is ENL = 15.

The aim of this section is to evaluate the L-band polarimetric behaviour of the sea in this scene. An easy way to display (part of) the information contained in quad-polarimetric acquisitions is by using a Pauli RGB colour composite image. The Pauli scattering vector is defined as $\mathbf{k_p}$, whose first component represents odd bounce (as surface scattering or trihedral corner reflectors), the second is an even bounce (as dihedrals corner reflectors horizontally oriented),

Table 6.6 Test sites and corresponding radar and validation data selected for the generation of showcases on ship detection

Application/Product	Test site – radar data	Reference data
Ship detection	Tokyo Bay, Japan	NDA reference data (video camera, ground radar, AIS)
	ALOS-PalSAR	

and the third is a dihedral with the corner 45 degree oriented along the Line of Sight (please note, in case of absence of target orientations, the latter is often exploited as an indicator of volume scattering). Figure 6.10 presents the RGB image of the test area with the overlapped "ground-surveyed" targets.

In this section, the visual interpretation is used as a benchmark to compare the algorithms with the results that could be provided by a SAR image analyst. In the following, green indicates detected targets, while red is for missing vessels. The circles are targets observed in the ground survey and visible in the RGB image, while the rectangles are vessels present in the survey but invisible in the RGB. The number beside the rectangles indicates that more vessels are closed to each other in the same area. The green curve delineates an area where seaweed farms (laver) are present. Please note there are also other coastal areas where laver cultivations are present, but they are not listed in the survey. The video camera and the ground radar were located close to the NDA (National Defence Academy) indicated by a black circle.

In the Pauli RGB [Fig. 6.10a], the sea is clearly distinguishable from other features in the scene due to its blue colour. The Bragg scattering model can be used to approximate the scattering from the sea surface at this frequency. An exception is when the sea state is particularly calm (or generally when the gravitational and capillary waves are dampened) leading to a backscattering proximal to the noise floor. In the image, many point targets in the sea area appear to present a clearly distinguishable polarimetric behaviour (i.e. different colours). In order to have an intuitive idea regarding possible advantages of using quad/polarimetric data, Fig. 6.10b presents the intensity of the HV channel (cross-polarization). The latter is often exploited to perform ship detection since, accordingly to the Bragg model, the cross-polarization should be negligible on the sea, therefore increasing the contrast between ships and sea. However, only using HV the visual discrimination between ships and sea becomes harder.

Further details regarding the sea polarimetric behaviour can be obtained applying the Cloude-Pottier decomposition. Figure 6.11 presents the resulting entropy and averaged α angle. As expected, the sea exhibits relatively low values of entropy indicating one dominant scattering mechanism. The averaged α is also small, indicating surface scattering. Finally, it is interesting to notice that in some sea areas, especially exhibiting low backscattering, the values of entropy and α increase. This is mainly due to noise effects.

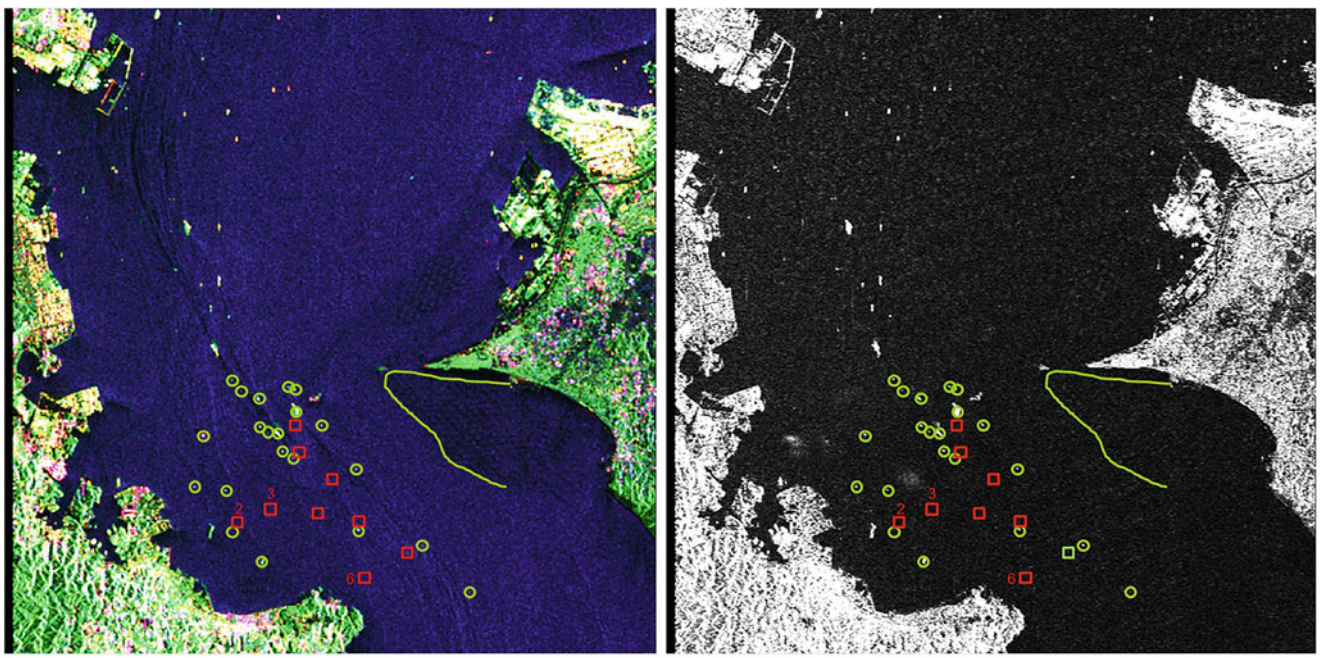

Fig. 6.10 RGB Pauli and HV intensity of the surveyed area, ALOS-PALSAR (JAXA), Tokyo Bay (35,294451; 139,785816). Green circles, targets present in the ground survey and visible in the RGB; red rectangles, vessels present in the ground survey but completely invisible in the RGB. The green curve delineates an area with seaweed (laver) cultivations. The video camera and the ground radar were located close to the NDA (National Defence Academy) indicated by a black circle. Incidence angle: ~24degrees. Multi-look: 1x5. Image size: 1000 × 1000 pixels, ~30 × 30 km

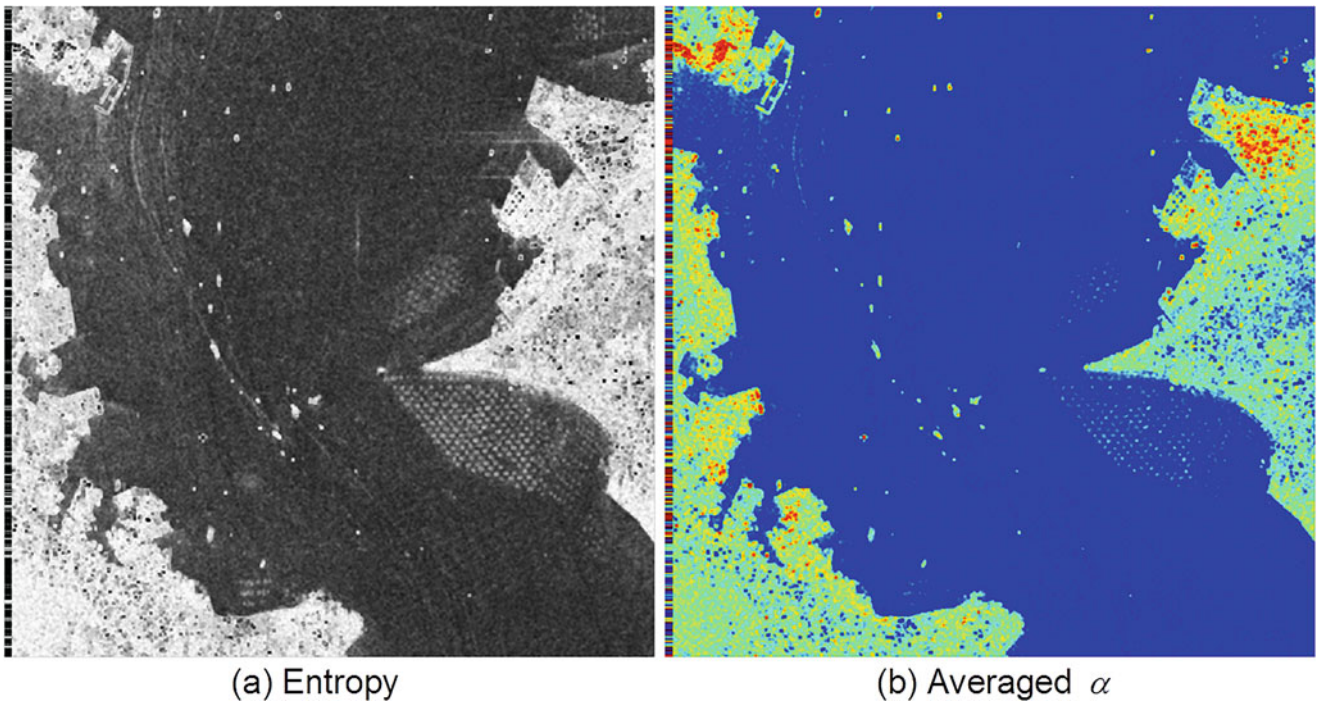

Fig. 6.11 Entropy and averaged α angle from the Cloude-Pottier decomposition. (**a**) Entropy, scaled between 0 and 1; (**b**) averaged α, scaled between 0 and $\pi/2$, blue-red (rainbow) colour bar

6.5.3 Detection with Quad-Polarimetric Data

The quad-polarimetric detectors compared in this section are the geometrical perturbation-polarimetric notch filter (PG-PNF) (Marino 2013), the polarimetric match filter (PMF) (Novak et al. 1989), the Liu et al. detector (Liu et al. 2005) and the polarimetric entropy.

Figure 6.12 presents the detection masks for each detector. The same circles and rectangles shapes extracted by the visual interpretation are represented on each detection masks in order to have a benchmark for algorithm comparison. The window size of the boxcar filter is 3×3 (after the 1×5 multi-look). The training for the detectors (i.e. the definition of the sea clutter backscattering) is performed manually choosing a representative area in the dataset. An operative solution may consider guard windows; however this is not presented here because it will generate a strong dependency of the results on the dimension of the selected guard window, which may obstruct a proper performance assessment. More details on the detector parameters are provided in the caption of Fig. 6.12. The results are summarized in Table 6.7, in the following only few comments are presented.

6.5.3.1 Detection

Interestingly, all the quad-polarimetric algorithms are able to detect the vessels visible in the RGB image except for the entropy that misses one. Moreover, they can detect one vessel identified in the survey but very hardly visible in the RGB.

6.5.3.2 Missing Detection

Several vessels were missing in the detection masks and visual interpretation. These are mainly small vessels, supposedly made of fibre glass. A finer sensor's spatial resolution may be a way to try to retrieve small targets. However, if a vessel is composed of materials almost transparent to the electromagnetic wave (e.g. absence of large metallic parts), it may still be physically impossible to observe it.

6.5.3.3 Seaweed

All the algorithms seem to be able to identify part of the laver seaweed farm. This is composed of nets lying on the sea surface. Entropy provides the best laver detection; it is followed by the PMF and the GP-PNF. Their detectability is physically based on the fact that the nets damp the Bragg resonant waves leading to a non-Bragg scattering. This is why the entropy is a good candidate to detect them. Please note that in the scene, other coastal areas present laver cultivations and are not indicated in the ground survey (but they can be detected by the entropy). Finally, Liu et al. is missing the most of the nets.

6.5.3.4 False Alarms

Unfortunately, the ground survey that accompanies the SAR data is not accurate enough to allow a reliable estimation. For instance, a vessel detected by the SAR and invisible to the video/radar (perhaps because too far from the NDA buildings) would be listed as false alarm. However, for

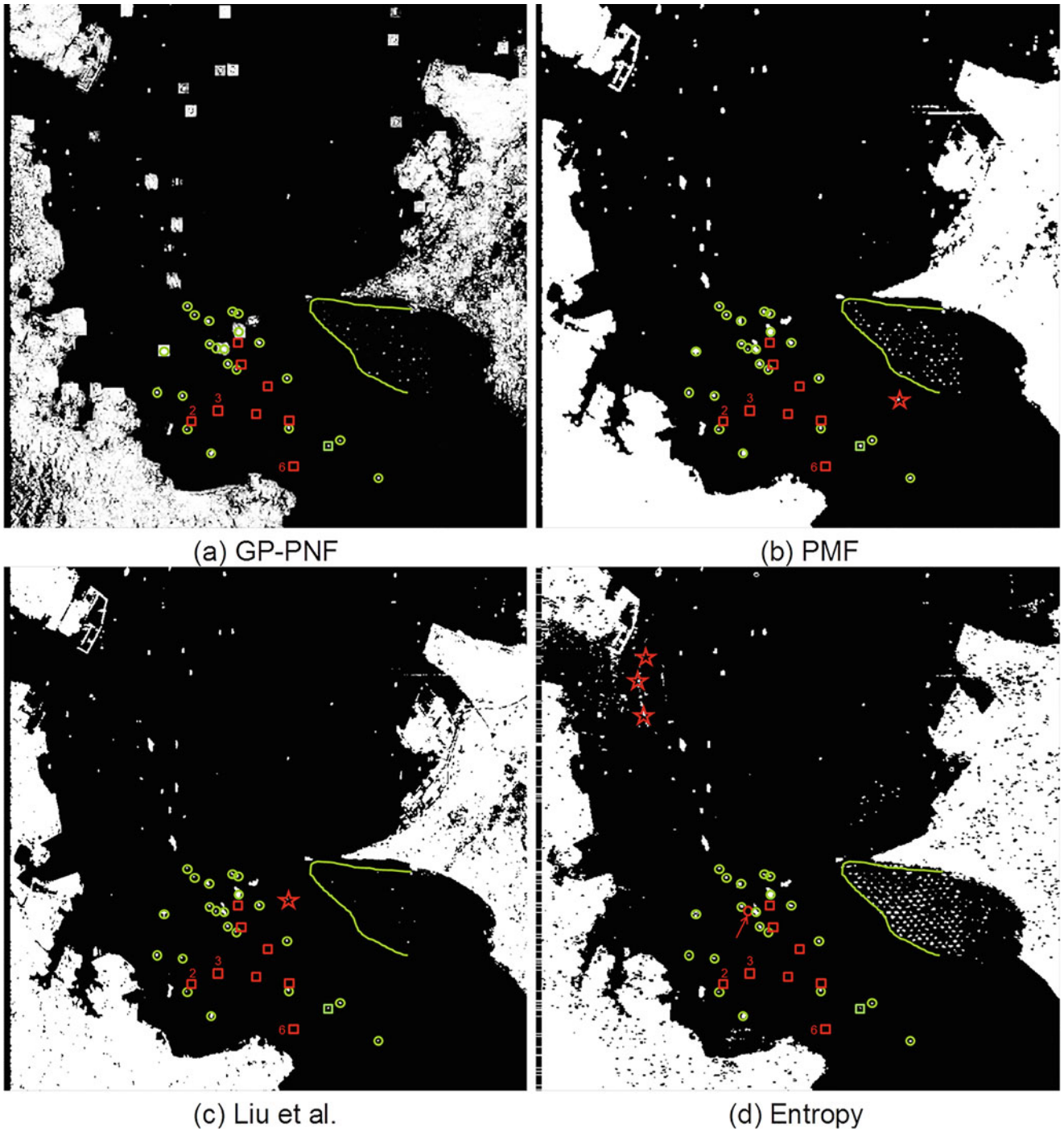

Fig. 6.12 Detection with quad-polarimetric data: (**a**) GP-PNF ($RedR = 10^{-4}$ and $T = 0.98$); (**b**) PMF ($T = 4$); (**c**) Liu et al. ($P_f = 10^{-4}$); (**d**) entropy ($T = 0.5$). Green, detected vessels; red, missing vessels. Red arrows: missing vessels that can be visually identified. Stars are supposed false alarms

Table 6.7 Detection results for the algorithms tested

Algorithms	Visual RGB	GP-PNF	PMF	Liu et al.	Entropy	Symmetry	HV
Detected	21	22	22	22	21	14	18
Missed	9(17)	8(16)	8(16)	8(16)	9(17)	16(24)	12(20)
False alarms	0	0	1	1	Several	0	0

what is observed in the test area, the GP-PNF does not present any false alarm, while the PMF and Liu et al. have one false alarm each. They are indicated in the images with stars. This result shows the robustness of such detectors. The entropy has no false alarms in the area close to NDA; however, many detections are located in areas exhibiting low backscattering. Some of them correspond to ships wakes and therefore can be easily defined as false alarms. A more thorough treatment of false alarms is provided in the final section when the receiver operating characteristic curves are presented.

6.5.4 Dual- and Single-Polarimetric Detectors

In this section, the results with the dual-polarimetric VV/VH symmetry detector (Nunziata et al. 2012b) and a CFAR test on the HV intensity exploiting the K-distribution (Crisp 2004) is presented. In this detection test, the threshold on the HV intensity is set solving numerically the integral for $P_f = 10^{-5}$ (exploiting a K-distribution). The threshold for the symmetry detector is 0.1, since this was shown to be a robust threshold selection over other datasets. As for the other detectors, the boxcar window is 3×3 after multi-look.

Figure 6.13 presents the detection masks for these two detectors, while the results are summarized in Table 6.7. It is evident that the detection performance is reduced substantially. Compared to the 22 vessels detected by the quad-pol algorithms, the HV intensity misses 4, and the symmetry misses 8 vessels. This numbers can be converted in relative degradation of the P_d obtaining 18% for the HV and 36% for the symmetry detector. The absolute degradations (when all the surveyed vessels are considered) are 13% and 26%. In particular, some ships visible in the RGB Pauli image are lost. Other tests were performed changing slightly the threshold in order to ensure the right setting of the detectors parameters. However, the number of detections increased only slightly. In the next section, an analysis is performed to assess the impact of a bad threshold selection to the lower detection performance. The area with seaweed farms is completely missing in the detection masks.

6.5.5 Receiving Operating Characteristics

The detection masks presented in the previous section help in understanding the detection capabilities in a more operational test, where one threshold is fixed. However, the threshold selection may be not optimal, and the poor performance of one algorithm may be just caused by a bad threshold selection. For this reason, it is valuable to assess the algorithms performance independently of the threshold selection. This can be accomplished plotting P_d against P_f and generating the so-called receiver operating characteristic (ROC) curves (Kay 1993). In this way, the problem of optimally selecting the threshold is de-coupled with assessing the best detector.

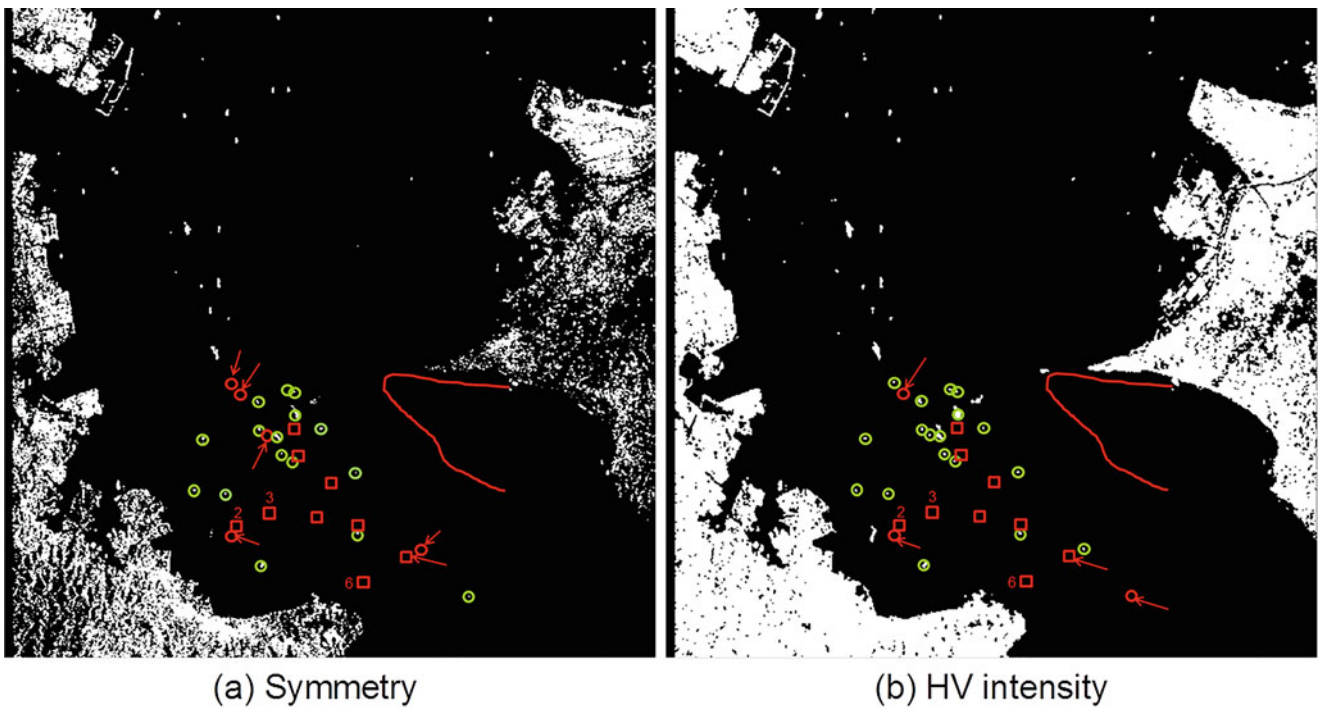

Fig. 6.13 Detection with dual- and single-polarimetric data: (**a**) symmetry detector ($T = 0.1$); (**b**) HV intensity ($P_f = 10^{-5}$). Green, detected vessels; red, missing vessels. Red arrows: missing vessels that can be visually identified. Stars are supposed false alarms

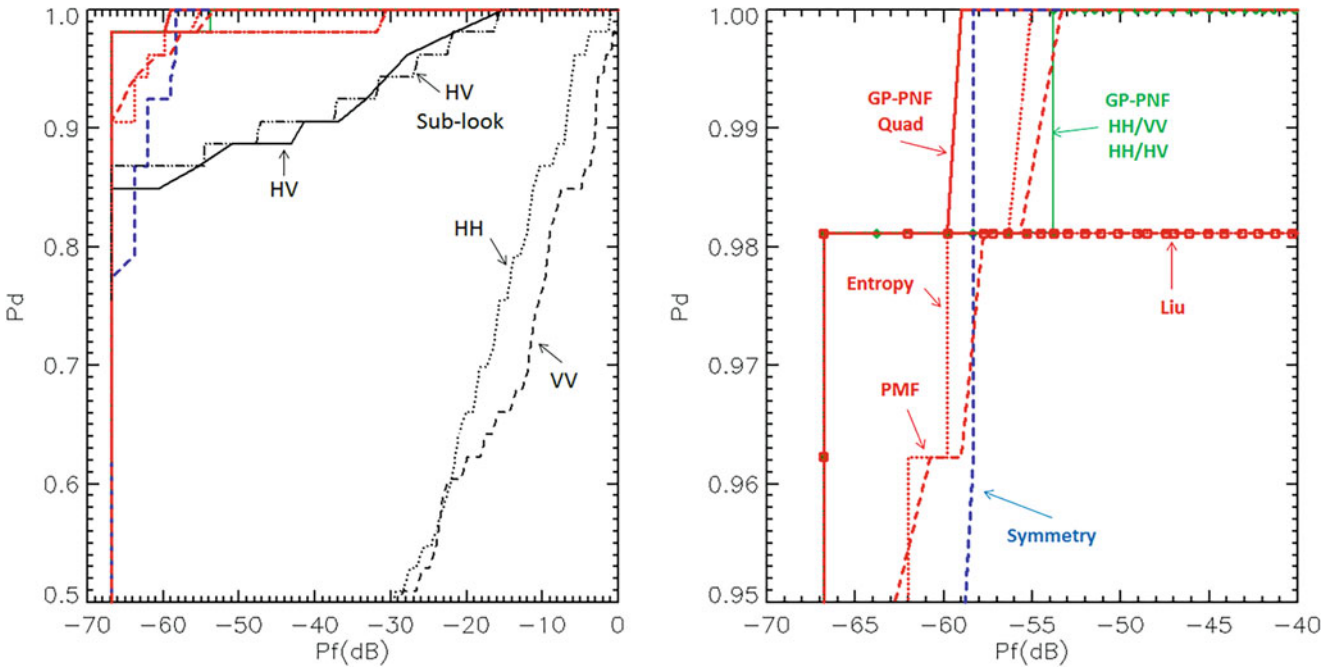

Fig. 6.14 ROC curves for the different detectors: red solid, GP-PNF quad-pol; red dotted, Cloude-Pottier entropy; red dashed, PMF; red squares, Liu et al.; blue dashed, symmetry VV/VH; green solid, dual-pol HH/VV GP-PNF; green diamonds, dual-pol HH/HV GP-PNF; black solid, HV intensity; black dotted, HH intensity; black dashed, VV intensity; black dot dash, cross-correlation of sub-look images in HV. (**b**) Presents a zoom of (**a**) in the upper left area. Best detection is in the upper left area of the plot

P_d is calculated only for visible vessels, since we were not able to assess the exact location of the pixels representing the missing vessels (i.e. the analysis is restricted to vessels that have some backscattering). In order to find a meaningful value for P_f, a large area in the dataset outside Tokyo Bay is selected where no apparent vessels were present.

Figure 6.14 shows the ROC curves for the different polarimetric detectors. As a comparison also the single-channel detectors using the intensity of HV, HH and VV are considered. Finally, in order to provide a more complete analysis a detector based on spectral (or sub-look) analysis of SAR data is presented (in the plot, it is indicated with HV sub-look, and a more complete name is sub-aperture cross-correlation magnitude). Details regarding the latter detector are not presented here for the sake of brevity, but they can be found in Brekke et al. (2013)). In very few words, this is a single-channel detector aiming at increasing the contrast between sea clutter and vessels because sea areas in different nonoverlapping portions of the image spectrum are uncorrelated. The sub-look detector tested here considered two nonoverlapping portions of the range spectrum with a 3×3 window.

Finally, two more detectors are considered in the ROC analysis. The GP-PNF is executed feeding the algorithm with only dual-polarimetric data (HH/VV and HH/HV). The idea behind this analysis is that keeping the same detector and feeding it with fewer images give a clear indication of how the loss of information impacts the detection performance.

As a final remark, the ROC curves presented here are different from the ones showed in [39] because the area used for estimating the false alarms is different. In [39], a region presenting a large area affected by azimuth ambiguities (coming from the nearby Tokyo) was selected in order to test the sensitivity of the detectors to such artefact. Here, the comparison between different polarimetric modes is investigated, and therefore including artefact may mask part of the differences (since it is never possible to obtain high P_d and low P_f due to the detection of the ambiguities).

Analysing the ROC curves, few conclusions can be drawn:

1. The best detectors seem to be the quad-polarimetric ones (red curves), followed by the dual-polarimetric ones (blue and green curves).
2. Among the single-polarimetric channels, the HV seems to be the best, followed by HH and finally VV. This can be found in the literature; however, there may be situations where the co-polarized channels may be more beneficial for detection (it depends on sea state and incidence angle).
3. The sub-look processing seems to not improve the HV detection in this test. A reason may be that the sea background is already quite low, and therefore the loss of resolution (due to sub-looking) is not paid back with a significantly better contrast.

4. The symmetry detector presents a very good ROC curve (not largely inferior to quad-pol detectors), but its P_d from the previous analysis was quite low. This is probably due to a wrong selection of the threshold, and therefore it should be possible to improve the detection mask with an algorithm able to select the threshold locally (or at least based on the specific dataset).

6.5.6 Discussion on the Role of Polarimetry and Conclusions

This section presented the comparison of quad-, dual- and single-pol detectors over a dataset acquired by ALOS-PALSAR and kindly provided by JAXA. The test area is Tokyo Bay, Japan, and during the acquisition, a ground survey was conducted. The latter was carried out with a video camera and a ground radar (in X-band) located beside the Nation Defence Academy (NDA) at 100 m over the sea level. The availability of such information allowed the evaluation of quantitative results. The quad-pol detectors tested here are the geometrical perturbation-polarimetric notch filter (GP-PNF), the polarimetric match filter (PMF), the Liu et al. and the entropy, while the dual-pol algorithm is the symmetry detector, and the single pol is a CFAR test on the HV intensity exploiting the K-distribution. Besides, a visual inspection was attempted on the RGB Pauli and the HV intensity images to provide a benchmark for the comparison of the other detectors.

The results showed that the quad-pol algorithms are able to detect 22 vessels (i.e. all the vessels visible in the RGB plus one), while the symmetry and HV suffer from more missed detections (respectively 14 and 18 vessels detected) which return a degradation of performances respectively of 13% and 26%. The false alarms are low for all the detectors tested at exception of the entropy detector which is not suitable in areas presenting low backscattering. Finally, a ROC curve analysis is performed with the purpose of assessing the detector performances independently of the threshold selection.

Some specific comments on the results are as follows:

1. Initially, it is interesting to notice that the use of quad-polarimetry is helpful to improve the detection capability even in the quite straightforward case of human interpretation. In Fig. 5.2 it can be observed that a smaller amount of vessels is distinguishable from the sea clutter in the HV intensity image alone.
2. All the quad-pol detectors perform in similar ways in the context of detection capability. This is an indicator that in this experiment, the main driver for the detection performance is quad-polarimetry (compared to dual-polarimetry) more than the specific detector or the selection of its parameters. Clearly, in other datasets a larger difference between the quad-pol detectors could be observed.
3. Analysing the ROC curves, the difference between quad- and single-pol detectors is large on this dataset, especially for the case of the co-polarizations. In the case of HV, a $P_d > 0.95$ can only be reached at the expenses of a $P_f > 10^{-3}$ (which is not appropriate for many applications).

6.5.7 Acknowledgement

The authors would like to thank the Japanese Aerospace Exploration Agency (JAXA) for the kind provision of the ALOS-PALSAR data.

6.6 Summary (Table 6.8)

Table 6.8 Summary of presented application, methods and preferred system configurations for ocean monitoring

Application	Methods and used frequency (P/L/C/X)	Radar data preference/requirements/comments
Oil observation	PolSAR features from T/C matrix for detection (L/X)	No preferred frequency Careful choice of incidence angle and noise floor for system design
	Unsupervised classification based on PolSAR features for classification of oil types (C/X)	
Metallic targets and ship detection	PolSAR detectors based on T/C matrix for metallic target detection (C)	No preferred frequency
	PolSAR detectors based on T/C matrix for ship detection (L)	

References

(2005) Aerial-surveillance – Cooperation on aerial surveillance over the North Sea area. In: Bonn Agreement Counter Pollution Manual

Brekke C, Solberg AHS (2008) Classifiers and confidence estimation for oil spill detection in ENVISAT ASAR images. IEEE Geosci Remote Sens Lett 5:65–69

Brekke C, Anfinsen SN, Larsen Y (2013) Subband extraction strategies in ship detection with the subaperture cross-correlation magnitude. IEEE Geosci Remote Sens Lett 10:786–790

Brekke C, Holt B, Jones C, Skrunes S (2014) Discrimination of oil spills from newly formed sea ice by synthetic aperture radar. Remote Sens Environ 4:1–14

Crisp DJ (2004) The state-of-the-art in ship detection in synthetic aperture radar imagery. Defence science and technology organisation, DSTO-RR-0272. [online]. http://www.dtic.mil/cgi-bin/GetTRDoc?AD=ada426096

Ferrara G, Migliaccio M, Nunziata F, Sorrentino A (2011) GK-based observation of metallic targets at sea in full-resolution SAR data: a multipolarization study. IEEE J Ocean Eng 36:195–204

Hühnerfuss H (2006) Basic physicochemical principles of monomolecular sea slicks and crude oil spills. In: Gade M, Hühnerfuss H, Korenowski GM (eds) Marine surface films. Springer, Berlin/Heidelberg

Jones CE, Minchew B, Holt B, Hensley S (2011) Studies of the deepwater horizon oil spill with the UAVSAR radar. Geophys Monogr Ser 195:33–50

Kay SM (1993) Fundamentals of statistical signal processing. Prentice Hall

Kotova LA, Espedal HA, Johannessen OM (1998) Oil spill detection using spaceborne SAR: a brief review. In: Proceedings of 1998 International Symposium on Remote Sensing of the Environment

Liu C, Vachon PW, Geling GW (2005) Improved ship detection with airborne polarimetric SAR data. Can J Remote Sens 31:122–131

Marino A (2013) A notch filter for ship detection with polarimetric SAR data. IEEE J Sel Top App Earth Obs Remote Sens 6:1219–1232

Migliaccio M, Nunziata F (2014) On the exploitation of polarimetric SAR data to map damping properties of the deepwater horizon oil spill. Int J Remote Sens 35:3499–3519

Migliaccio M, Gambardella A, Nunziata F, Shimada M, Isoguchi O (2009a) The PALSAR polarimetric mode for sea oil slick observation. IEEE Trans Geosci Remote Sens 47:4032–4041

Migliaccio M, Nunziata F, Gambardella A (2009b) On the co-polarised phase difference for oil spill observation. Int J Remote Sens 30:1587–1602

Migliaccio M, Nunziata F, Montuori A, Brown CE (2011a) Marine added-value products by RADARSAT-2 fine quad-polarization mode. Can J Remote Sens 37:441–450

Migliaccio M, Nunziata F, Montuori A, Li X, Pichel W (2011b) A multifrequency polarimetric SAR processing chain to observe oil fields in the Gulf of Mexico. IEEE Trans Geosci Remote Sens 49:4729–4737

Minchew B, Jones CE, Holt B (2012) Polarimetric analysis of backscatter from the deepwater horizon oil spill using L-band synthetic aperture radar. IEEE Trans Geosci Remote Sens 50:3812–3830

Novak LM, Sechtin MB, Cardullo MJ (1989) Studies of target detection algorithms which use polarimetric radar data. IEEE Trans Aerosp Electron Syst 25:150–165

Nunziata F, Migliaccio M (2013) On the COSMO-SkyMed PingPong mode to observe metallic targets at sea. IEEE J Ocean Eng 38:71–79

Nunziata F, Gambardella A, Migliaccio M (2008) On the Mueller scattering matrix for SAR oil slick observation. IEEE Geosci Remote Sens Lett 5:691–695

Nunziata F, Migliaccio M, Gambardella A (2011) Pedestal height for oil spill observation. IET Radar Sonar Navigation 5:103–110

Nunziata F, Gambardella A, Migliaccio M (2012a) A unitary Mueller-based view of polarimetric SAR oil slick observation. Int J Remote Sens 33:6403–6425

Nunziata F, Migliaccio M, Brown CE (2012b) Reflection symmetry for polarimetric observation of man-made metallic targets at sea. IEEE J Ocean Eng 37:384–394

Nunziata F, Migliaccio M, Li X (2015) Sea oil slick observation using hybrid-polarity SAR architecture. IEEE J Ocean Eng 40:426–440

Raney RK (2011) A perspective on compact polarimetry. IEEE Geosci Remote Sens Newslett 160:12–18

Reed M et al (1999) Oil spill modeling towards the close of the 20th century: overview of the state of the art. Spill Sci Technol Bull 5:3–16

Salberg AB, Rudjord, Ø, Solberg AHS (2012) Oil spill detection in compact polarimetry SAR images. Paper presented at ESA SeaSAR 2012

Shirvany R, Chabert M, Tourneret JY (2012) Ship and oil-spill detection using the degree of polarization in linear and hybrid/compact dual-pol SAR. IEEE J Sel Top Appl Earth Obs Remote Sens 5:885–892

Skrunes S, Brekke C, Eltoft T (2012a) An experimental study on oil spill characterization by multi-polarization SAR. In: Proceedings of 2012 European Conference on Synthetic Aperture Radar (EUSAR)

Skrunes S, Brekke C, Eltoft T (2012b) A comprehensive analysis of polarimetric features for oil spill characterisation. Paper presented at ESA SeaSAR 2012

Skrunes S, Brekke C, Eltoft T, Kudryavtsev V (2015) Comparing near-coincindent C- and X-band SAR acquisitions of marine oil spills. IEEE Trans Geosci Remote Sens 53:1958–1975

Solberg AHS (2012) Remote sensing of ocean oil-spill pollution. Proc IEEE 100:2931–2945

Touzi R, Charbonneau F (2002) Characterization of target symmetric scattering using polarimetric SARs. IEEE Trans Geosci Remote Sens 40:2507–2516

Velotto D, Migliaccio M, Nunziata F, Lehner S (2011) Dual-polarized TerraSAR-X data for oil-spill observation. IEEE Trans Geosci Remote Sens 49:4751–4762

Wenguang W, Fei L, Peng W, Jun W (2010) Oil spill detection from polarimetric SAR image. In: Proceedings of IEEE 2010 International Conference on Acoustic Speech Signal Processing (ICASSP)

Yeremy M, Campbell JWM, Mattar K, Potter T (2001) Ocean surveillance with polarimetric SAR. Can J Remote Sens 27:328–344

Zhang B, Perrie W, Li X, Pichel GP (2011) Mapping Sea surface oil slicks using RADARSAT-2 quad-polarization SAR image. Geophys Res Lett 38:1–5